POLITECNICO MILANO 1863

SCUOLA DI INGEGNERIA INDUSTRIALE E DELL'INFORMAZIONE

Constitutive Modeling of 3D Printed Tough Resin

TESI DI LAUREA MAGISTRALE IN MECHANICAL ENGINEERING INGEGNERIA MECCANICA

Author: **Yongcun Zhou**

Student ID: 10551609
Advisor: Antonio Mattia Grande
Co-advisor: Bianca Omede
Academic Year: 2024-2025

Abstract

This thesis investigates the large-deformation mechanical behaviour and constitutive modelling of a commercial vat-photopolymerized resin—Anycubic Tough Resin Ultra—under varying strain rates and temperatures. A series of uniaxial tension and compression, stress relaxation, and cyclic loading experiments were conducted across multiple thermal conditions, revealing significant viscoelasticity, hydrostatic pressure dependence and Mullins effect. Fracture surface analysis indicated that the material predominantly operates in the glassy state, exhibiting nonlinear viscoelasticity with limited plasticity.

Building upon foundational models such as the Bergström–Boyce and Three-Network frameworks, four constitutive models were evaluated, including the Ansys Bergström–Boyce, Ansys Three Network model, Abaqus PRF, and the PolyUMod Three Network Viscoplastic (TNV) model. Among these, the PolyUMod TNV model with Mullins effect exhibited the best overall accuracy in capturing hysteresis loops, residual strain, and strain hardening. Temperature-dependent parameters were extracted at discrete points and interpolated using PolyUMod multi-temperature framework.

The calibrated model was implemented in LS-DYNA and validated through numerical simulations of cyclic and monotonic loading both in tension, compression and Three points bending. The simulation results showed good agreement with experimental data, confirming the model's robustness across a range of conditions.

This work provides a calibrated, physically-consistent, and numerically efficient material model for tough photocurable resins, facilitating their use in structural simulation and engineering design applications involving additive manufacturing.

Keywords: vat photopolymerization, nonlinear viscoelasticity, constitutive modelling, PolyUMod TNV, Mullins effect, temperature dependence, LS-DYNA.

Abstract in Italiano

Questa tesi indaga il comportamento meccanico a grande deformazione e la modellazione costitutiva di una resina commerciale fotopolimerizzata in vasca — Anycubic Tough Resin Ultra — sottoposta a diverse velocità di deformazione e temperature. È stata condotta una serie di prove sperimentali, tra cui trazione e compressione uniaxiale, rilassamento degli sforzi e cicli di carico, in differenti condizioni termiche, che hanno rivelato una marcata viscoelasticità, una dipendenza dalla pressione idrostatica e un evidente effetto Mullins.

A partire da modelli fondamentali come Bergström–Boyce e il Three-Network framework, sono stati valutati quattro modelli costitutivi: Ansys Bergström–Boyce, Ansys Three Network, Abaqus PRF e PolyUMod Three Network Viscoplastic (TNV). Tra questi, il modello PolyUMod TNV con effetto Mullins ha mostrato la migliore accuratezza complessiva nel riprodurre i cicli di isteresi, la deformazione residua e l'indurimento da deformazione. I parametri dipendenti dalla temperatura sono stati ricavati in punti discreti e interpolati utilizzando l'infrastruttura multi-temperatura di PolyUMod.

Il modello calibrato è stato implementato in LS-DYNA e validato tramite simulazioni numeriche di carichi monotoni e ciclici in trazione, compressione e flessione a tre punti. I risultati numerici hanno mostrato un buon accordo con i dati sperimentali, confermando la robustezza del modello in un ampio range di condizioni.

Questo lavoro fornisce un modello costitutivo calibrato, fisicamente coerente ed efficiente dal punto di vista numerico per resine fotopolimeriche ad alte prestazioni, facilitandone l'utilizzo nella simulazione strutturale e nella progettazione ingegneristica nel contesto della manifattura additiva.

Parole chiave: fotopolimerizzazione in vasca, viscoelasticità non lineare, modellazione costitutiva, PolyUMod TNV, effetto Mullins, dipendenza dalla temperatura, LS-DYNA.

Contents

Introduction

Additive manufacturing (AM) has rapidly emerged as a transformative fabrication technology, offering significant advantages over conventional manufacturing methods in terms of cost efficiency, production speed, and design flexibility. Unlike traditional subtractive processes that require mold or extensive machining, AM enables the layer-by-layer construction of parts directly from digital models, reducing material waste and accelerating product development. The ability to customize geometries without additional tooling makes AM particularly suitable for small-batch production, rapid prototyping, and complex functional components.

Among various AM technologies, vat photopolymerization techniques—such as Stereolithography (SLA) and Digital Light Processing (DLP)—are widely used to fabricate high-resolution polymeric components using photocurable resins. These techniques have found broad applications in fields ranging from dental implants and microfluidic devices to structural prototypes and soft robotics. Their popularity stems not only from their precision but also from the tunability of material behaviours through parameters such as light intensity, exposure time, and layer thickness.

However, despite the increasing use of commercial resins, the mechanical behaviours of such materials remain insufficiently understood. Since the performance of printed parts is closely tied to the resin's viscoelastic, temperature and hydrostatic pressure sensitivities, a reliable material model is essential for predictive simulations and engineering design. In recent years, a new generation of tough photocurable resins—such as Anycubic Tough Resin Ultra, Siraya Tech Blu-Tough Resin, and Formlabs Durable V2—has been developed, offering significantly enhanced strength, ductility, and fracture resistance compared to conventional printing materials. These advancements have expanded the potential of resin-based AM in load-bearing and functionally demanding applications. At the same time, the improved performance introduces new challenges for accurate prediction and control, particularly under complex loading scenarios or extreme environmental conditions. Therefore, systematic experimental characterization and constitutive modelling are essential to fully unlock the potential of these materials and ensure their safe and effective use in structural applications.

A foundational contribution to polymer modelling was made by Ellen Arruda and Mary Cunningham Boyce in 1990s, who proposed the eight-chain hyperelastic model to describe the large deformation behaviours of polymer networks based on statistical mechanics. Building on this, Jorgen Bergstrom developed the Bergstrom–Boyce (BB) model, which introduced a two-network formulation that couples nonlinear elasticity with rate-dependent viscous flow, enabling accurate prediction of time-dependent behaviours in thermoplastic elastomers. To further improve modelling fidelity for materials exhibiting both viscoelastic relaxation and irreversible deformation, subsequent studies proposed three-network models. These extend the BB framework by introducing an additional network branch—often associated with viscoplastic flow or long-term structural reconfiguration—allowing for a clearer distinction between recoverable time-dependent behaviours and permanent deformation.

In this thesis, we developed a constitutive model that combines hyperelasticity with nonlinear viscoelasticity to describe the large deformation behaviours of Anycubic Tough Resin Ultra. The model parameters were identified through a series of mechanical tests, including uniaxial tension, compression, stress relaxation, and cyclic loading. To assess its predictive capability, the model was implemented into a finite element simulation environment and validated against the mechanical response of representative printed structures. This work aims to provide a physically consistent and numerically implementable model for photocurable resins, supporting their use in mechanical performance analysis and structural design in engineering applications.

1 Material Test

1.1. Specimen preparation

The specimens were fabricated using Anycubic Tough Resin Ultra in grey color, printed with the Phrozen Sonic Mighty 8K printer (Fig 1.1a), in accordance with the ASTM D638 Type I Standard (Standard No. 38066) and ASTM D695 (Standard No. 38608), then cured and washed by Anycubic Wash Cure 3 Plus (Fig 1.1b).

(a) (b)

Figure 1. 1 Specimen Preparation Apparatus

The specimen dimensions are shown in Figure 1.2 (a) and 1.2 (b).

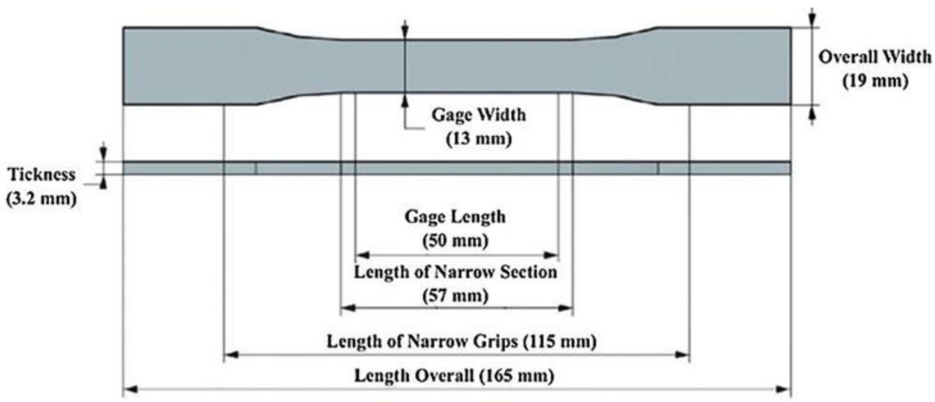

Figure 1. 2(a) ASTM D638 Type I Specimen

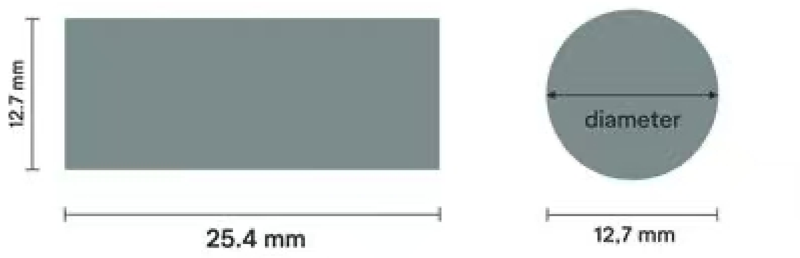

Figure 1. 2 (b) ASTM D695 Cylinder Specimen

The resin parameters are summarized in Table 1.1.

Table 1. 1 Resin Parameters

Property	Value
UV wavelength	365–405 nm
Elongation at break	70–80%
Density	1.05–1.25 g/cm³
Molding shrinkage	5.1–6.2%
Viscosity	500–900 cP·mPa·s
Flexural strength	15–25 MPa
Hardness	71–75 D
Flexural modulus	350–800 MPa
Bottom exposure time	20–40 s
Normal exposure time	1.5–3 s
Heat deflection temp	50–55 °C
Resin wash	Alcohol
Tensile strength	20–28 MPa
Conservation period	1.5 year

According to the manufacturer's recommendation, the printing process was carried out using the parameters listed in Table 1.2.

Table 1. 2 Recommended Printing Parameters

Property	Value
Layer Thickness	0.05 mm
Exposure Time	2 s
Light-Off Time	2 s
Bottom Exposure Time	25 s
Bottom Layer	4
Anti-Aliasing Level	1
Z Lift Distance	8 mm
Z Lift Speed	6 mm/s
Z Retract Speed	6 mm/s

After printing, the specimens were washed in 95% ethanol and post-cured for 10 minutes using the Anycubic Wash & Cure 3 Plus system. Following curing, they were stored in a black, sealed container at room temperature to prevent light exposure and slow down potential aging or degradation [2].

1.2. Experiment setup

The tensile tests were performed using an MTS C43 Criterion® Electromechanical Test System with a load cell of 50 kN (Figure 1.3), equipped with a temperature-controlled environmental chamber for multi-temperature tests. Strain was measured using MTS 632 Enhanced Travel Axial Extensometer (Figure 1.4) or MTS 634.25F-24 Large-Strain Axial Extensometer, each with a gauge length of 50 mm.

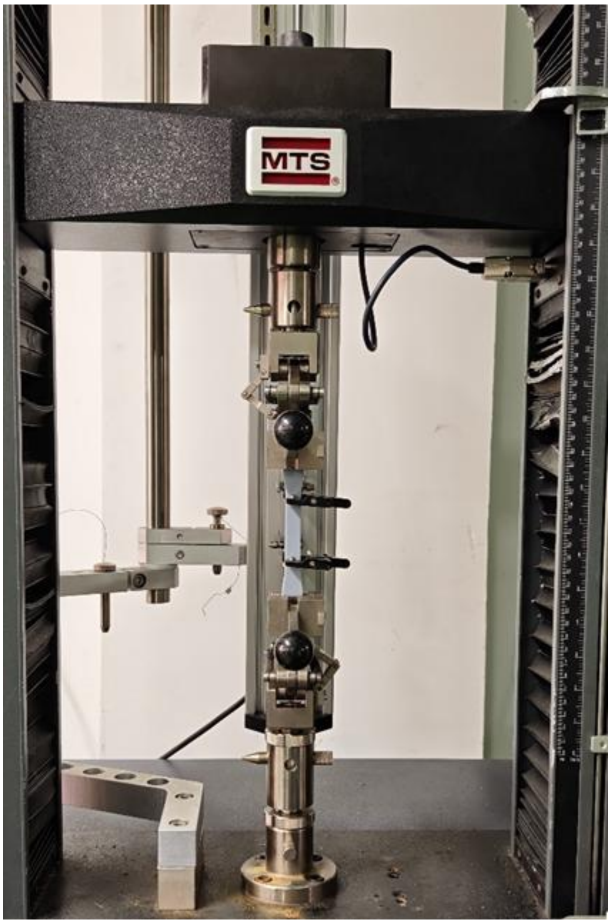

Figure 1. 3 Experiment Setup

Figure 1. 4 MTS Extensometer

The compression tests were performed using the same MTS C43 Criterion® Test System, but with a load cell of 100 kN (Figure 1.5), equipped with temperature-controlled environmental chamber for multi-temperature tests.

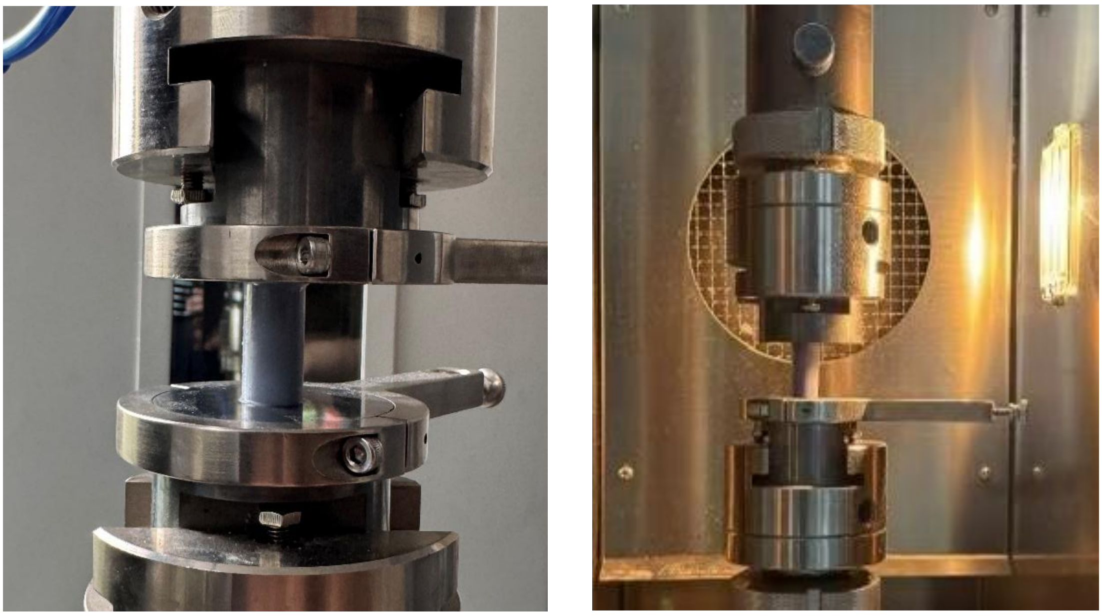

Figure 1. 5 Compression Test Setup

1.3. Preliminary Investigations

A series of preliminary tensile tests were conducted to evaluate the basic mechanical properties of the printed resin and to determine the candidate material models for the formal experiment procedure. The tests are designed to investigate:

(1) Anisotropy
(2) Strain rate dependency
(3) Viscoelastic response
(4) Temperature dependency
(5) Hydrostatic Pressure dependency
(6) Mullins Effect

1.3.1. Anisotropy

Although SLA-printed parts are generally considered nearly isotropic due to the covalent bonding formed during the curing process [1], experimental verification was still conducted in two print orientations (Figure 1.6). The horizontal and vertical printed specimens were denoted as TO and TV series respectively.

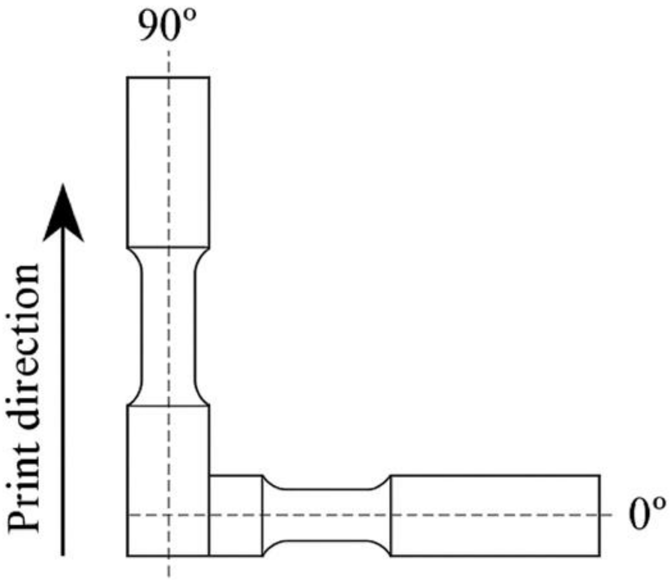

Figure 1. 6 Horizontal and Vertical Print Direction

The quasi-static engineering stress strain curves of TO and TV series are closely overlapped and appear interleaved throughout the deformation process (Figure 1.7). This intermingling of data from different directions suggests a negligible directional dependence, thus confirming the near-isotropic behaviour of the material under the tested conditions, and supporting the isotropy assumption used in the modelling framework.

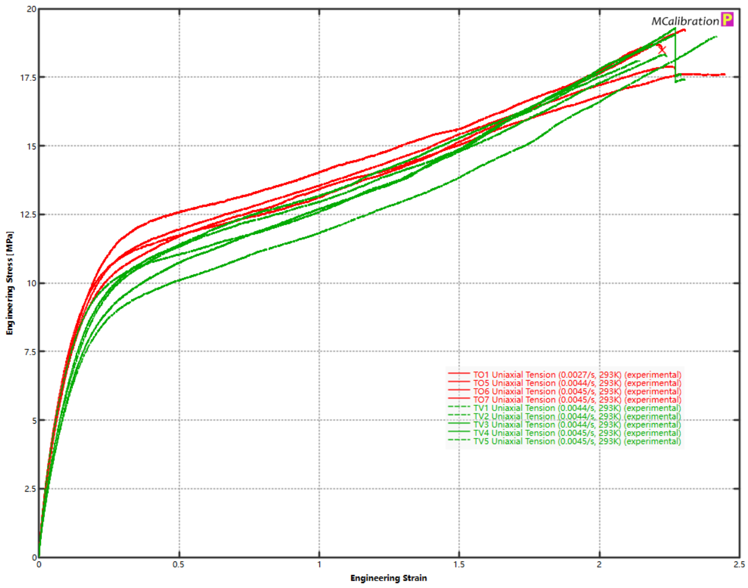

Figure 1. 7 TO and TV series specimen stress strain

1.3.2. Strain rate dependency

Monotonic tensile tests at room temperature were performed, the result at different strain rates are shown in Figure 1.8(a), the corresponding engineering strain rates vs engineering strain are plotted in Figure 1.8(b). Obviously, there exist a strong correlation, the yielding stress, flow stress and Young's modulus increase with the increasing of strain rate.

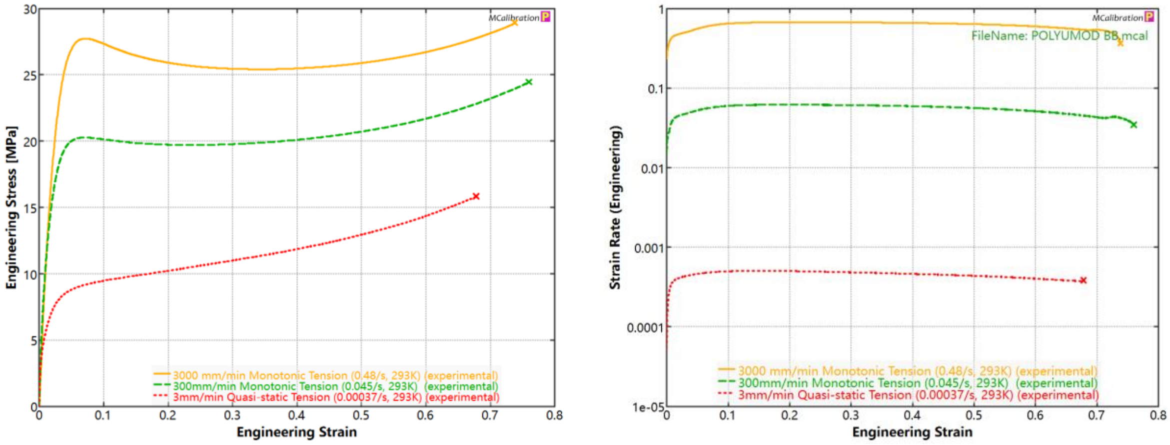

(a) (b)

Figure 1. 8 Engineering Stress vs Engineering Strain of different strain rates

As demonstrated in the high strain rate test (3000 mm/min), the stress–strain curve displays a distinct strain softening behaviour beyond the peak stress. This phenomenon is not observed under quasi-static loading but becomes increasingly evident as the strain rate rises. Besides, the slope immediately after the onset of inelastic flow decreases with strain rate, this indicates a viscous strain softening [2]. Therefore, to ensure predictive accuracy, the constitutive model should account for strain softening mechanisms.

1.3.3. Viscoelastic response

In order to observe the material's viscoelastic behaviour, cyclic loading tests with intermediate holding periods were conducted. This approach enables the identification of stress relaxation, hysteresis and inelastic deformation effects under repeated loading conditions.

A cyclic loading test was conducted at a cross-head speed of 3 mm/min, including several stress relaxation segments during the loading phase and one relaxation segment during the final unloading stage. The strain control history and engineering stress–strain is shown in Figure 1.9 (a) (b) and (c), alongside a quasi-static monotonic tensile test conducted at the same loading speed for comparison. In Figure 1.9(b), an increase of stress was observed in the unloading relaxation phase, suggesting viscoelastic recovery. This phenomenon is typical of viscoelastic polymers, in which the internal molecular network retains stored energy and continues to recover toward an equilibrium configuration after unloading. Figure 1.9 (c) reveal the phenomenon more clearly, from 3300 s to 3900 s, although the engineering strain was kept at 0.3, the engineering stress is increasing. Furthering observation of the relaxation segments shows after a relaxation of 600 seconds, the nominal stress magnitude is nearly halved, this strong relaxation behaviour suggesting the resin is quite viscoelastic.

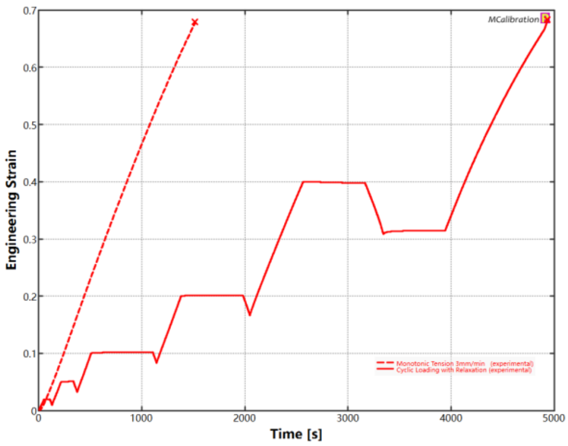

(a) Strain vs Time

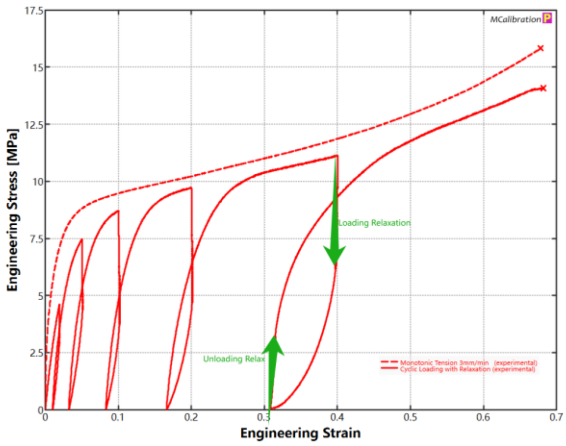

(b) Strain vs Stress

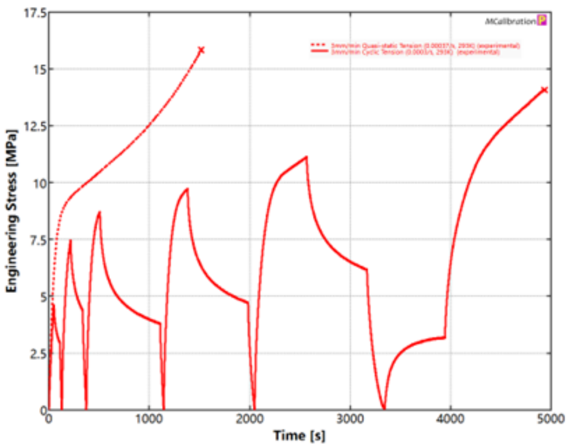

(c) Stress vs Time

Figure 1. 9 Quasi Static and Cyclic Loading of 3 mm/min

1.3.4. Temperature Dependency

According to the manufacturer's datasheet, the heat deflection temperature (HDT) of Anycubic Tough Resin Ultra ranges between 50 °C and 55 °C. Therefore, the selected test temperatures were intentionally kept below this range.

To investigate the temperature dependency of the material, a series of quasi-static tensile tests were conducted at 5 °C, 23 °C, 35 °C and 45 °C respectively. The resulting stress–strain curves under different thermal conditions are shown in Figure 1.10.

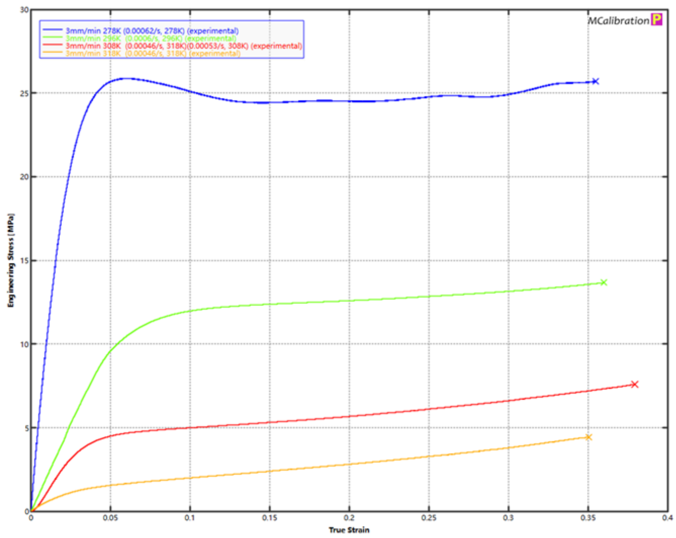

Figure 1. 10 Quasi-static tensile tests of different temperatures

As observed, increasing the temperature leads to a noticeable decrease in initial stiffness, yielding stress and flow stress, indicating that the material becomes softer and more ductile at elevated temperatures.

Further comparison of the ultimate tensile strength (UTS) and initial stiffness at different temperatures (see Figure 1.11 (a) and (b)) reveals a quasi-linear dependence on temperature.

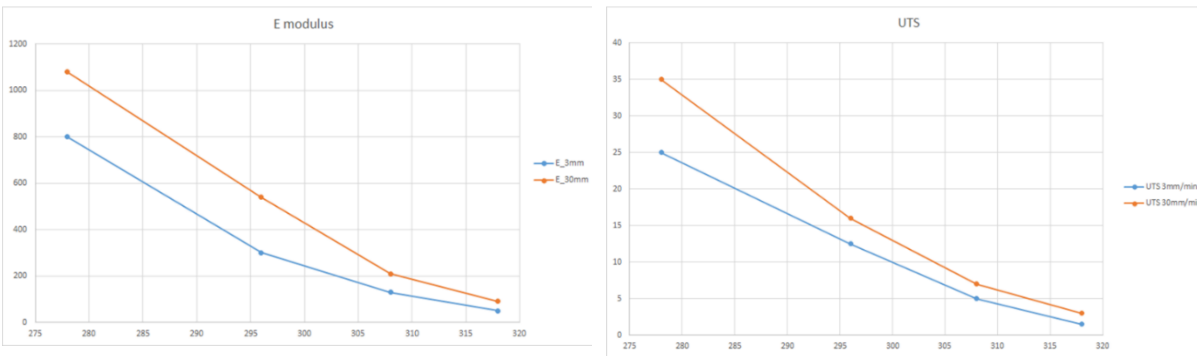

(a) (b)

Figure 1. 11 Young's Modulus and UTS vs Temperature

This observation suggests that the material model can be individually calibrated at several discrete temperatures, therefore the corresponding parameters can then be linearly interpolated over the tested temperature range to predict intermediate responses. Such an approach allows for temperature dependent modelling without introducing any additional complexity, while maintaining relatively good precision.

1.3.5. Hydrostatic Pressure

The mechanical behaviour of the SLA-printed resin exhibits pressure sensitivity [16], the material shows a higher yield stress in compression than in tension under comparable conditions. This behaviour is attributed to the influence of hydrostatic pressure: compressive loading introduces positive hydrostatic stress, which suppresses void nucleation and delays yielding. In contrast, tensile loading generates negative hydrostatic stress, promoting damage initiation. This asymmetry between tensile and compressive strength must be considered in structural applications involving multiaxial stress states. Compression tests were conducted in room temperature to investigate the hydrostatic pressure dependency preliminarily and the test result is shown in Figure 1.12. To eliminate friction effects during the compression test, lubricant was applied between the specimen surfaces and the upper and lower loading platens.

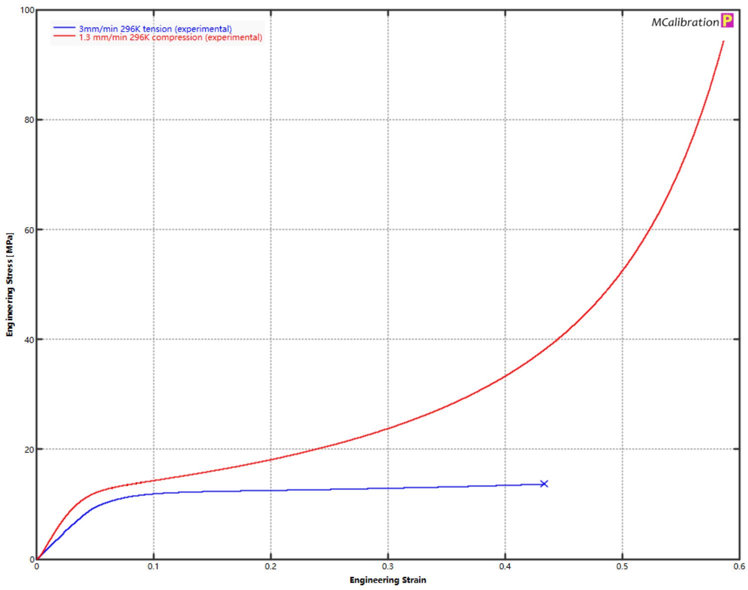

Figure 1. 12 Quasi Static Tension and Compression

As it shows in Figure 1.12, although the compression was conducted at 1.3mm/min (nominal strain rate 0.0008 s^{-1}) according to ASTM D695 standard, which is slightly lower than tensile test nominal strain rate (0.001 s^{-1}), the stiffness, yielding stress and UTS in compression is higher than in tensile test.

1.3.6. Mullins Effect

Cyclic tensile tests were carried out at different temperatures (278 K, 296 K, 308 K, 318K) and two strain rates (3 mm/min and 30 mm/min), using the same strain-controlled method. Figure 1.13 clearly illustrates the Mullins effect: in each cycle, the stress at a given strain decreases relative to the previous cycle. In both Figure 1.13 (varying temperature) and Figure 1.14 (varying strain rate), the engineering strain at zero stress after unloading remains consistent at 0.02, 0.05 and 0.13 respectively, despite large differences in strain rate or temperature. This suggests that the residual strain is not significantly affected by temperature and strain rate, as we know the viscoelasticity is typically sensitive to temperature and strain rate, this implies that the residual strain is primarily governed by Mullins effect, rather than being governed by viscoelastic networks.

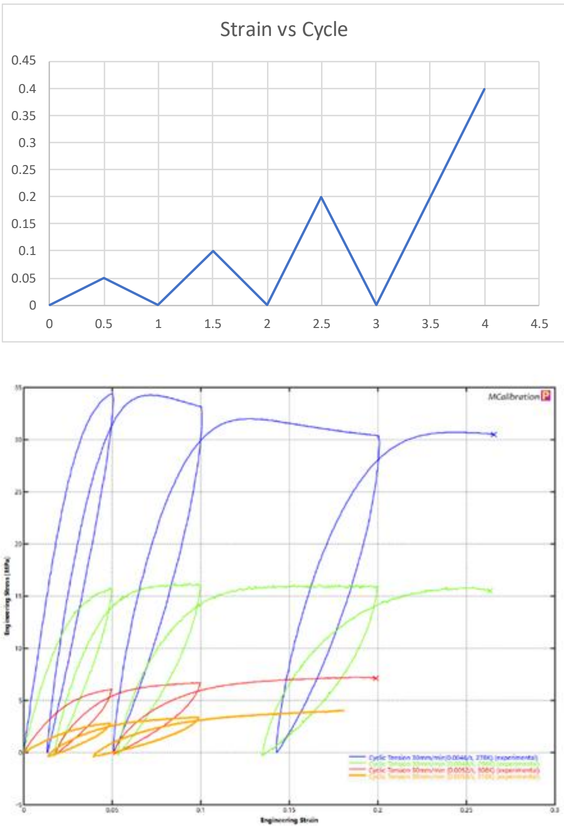

Figure 1. 13 Cyclic loading at different temperature

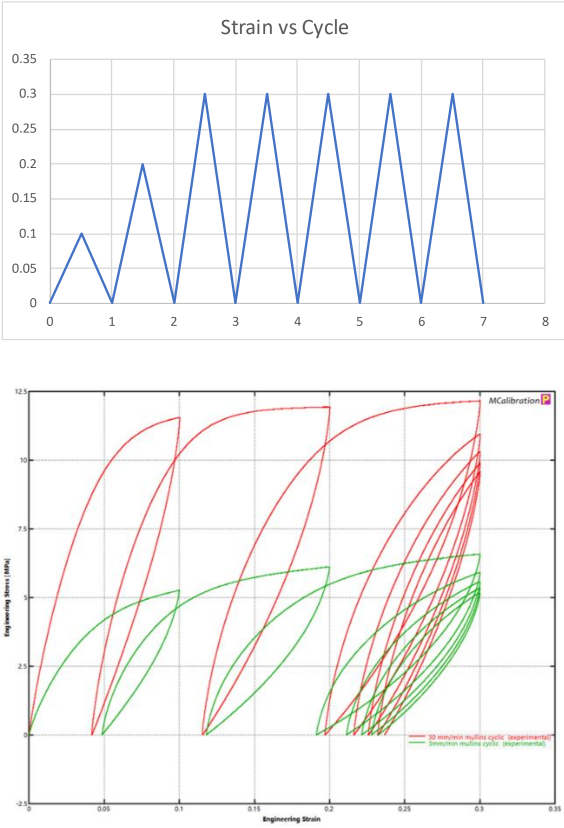

Figure 1. 14 Cyclic loading and Mullins Effect of different strain rate

1.4. Fracture and Post fracture observations

Under high-temperature and low-strain rate, the material exhibits good flowability, leading to noticeable but negligible necking. This is due to the increased molecular chain mobility at elevated temperatures, allowing the chains to slide and rearrange more easily, thereby facilitating larger strains in the necked region. Conversely, at low temperatures and high strain rates, the material's flowability is significantly reduced. The molecular chains cannot disentangle efficiently, and plastic deformation is limited, resulting in negligible necking.

Conclusively, necking is not a dominant feature under most experimental conditions, particularly at low temperatures and high strain rates. Instead, brittle fracture predominates, and the contribution of brittle fracture increases as the temperature decreases or the strain rate increases, as the material's molecular mobility is further hindered, leading to a more brittle failure with smoother, more abrupt fracture surfaces.

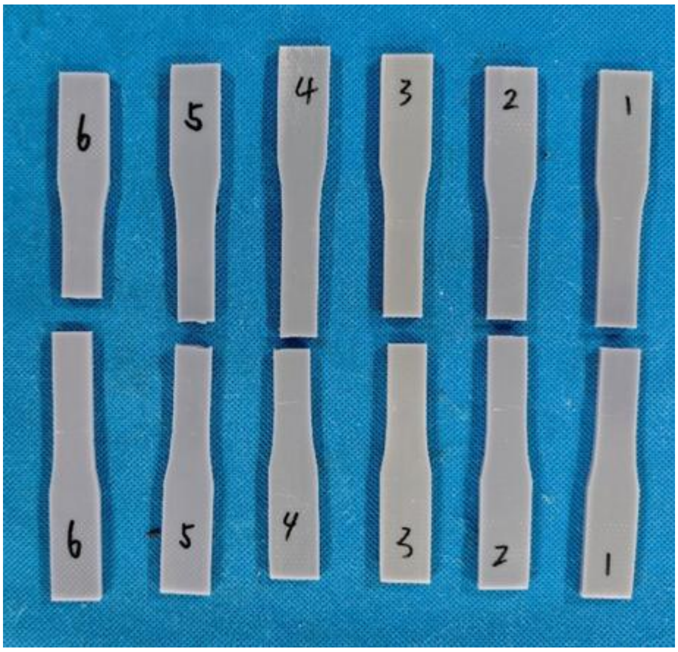

Figure 1. 15 Brittle Fracture under moderate strain rate

As shown in Figure 1.15, although the specimens experienced a large overall strain prior to failure, indicating significant deformability, the final fracture surface exhibits characteristic of brittle failure.

Under high-speed tensile testing, the fracture typically initiates near the gripping ends of the specimen (Figure 1.16). This is likely due to the reflection and superposition of stress waves at the clamps, causing localized stress concentrations near gripping ends. The rapid loading conditions result in stress wave propagation through the material, with the regions near the grips experiencing the highest stress due to wave reflection, leading to early failure in these areas. This phenomenon is consistent with Kolsky's stress wave theory [4], where the propagation and reflection of stress waves in high-speed tests can induce premature failure, especially at the clamping interface where stress is not uniformly distributed.

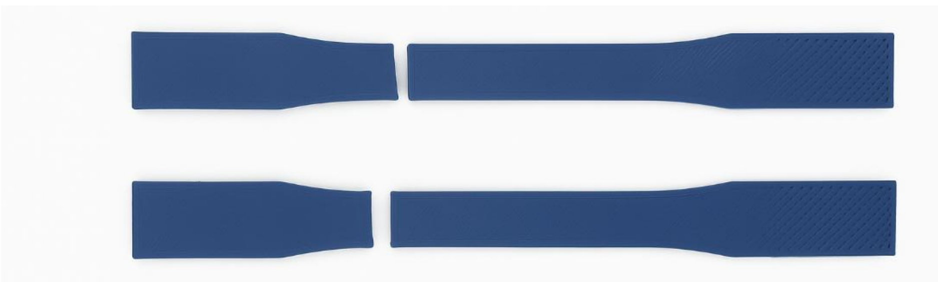

Figure 1. 16 Fracture of high strain rate test

Upon observation, immediately after fracture, both the upper and lower fragments underwent a rapid elastic recoil—each segment shortened by approximately 10 mm within seconds. In addition to standard mechanical testing, the room temperature experiments also included tracking of specimen length after fracture, the total average length of the fractured segments was recorded at multiple time intervals (10 min, 20 min, 30 min, 1 h, 2 h, 4 h, 8 h, 24 h, and 48 h), aimed to assess strain recovery and identify any delayed elastic or viscoelastic effects that may persist after rupture. The initial specimen length was 166.45 mm, at the moment of fracture, the axial displacement reached 38.2 mm, indicating that the full specimen length prior to failure was 204.65 mm. Meanwhile, the extensometer recorded an elongation of 27.26 mm, it is about 10 mm less than the crosshead displacement, reflects the contribution of deformation not only in the gauge section, but also in the shoulder and grip regions.

As shown in Figure 1.17, the initial post-fracture length, measured immediately after removing the specimen from the grips was 179.32 mm, it decreased to 176.87 mm after 600 seconds and continued to contract, eventually stabilized at approximately 168 mm after 48 hours. The absence of a significant permanent set indicates pronounced viscoelastic recovery, suggesting that the material exhibits elastomeric behavior.

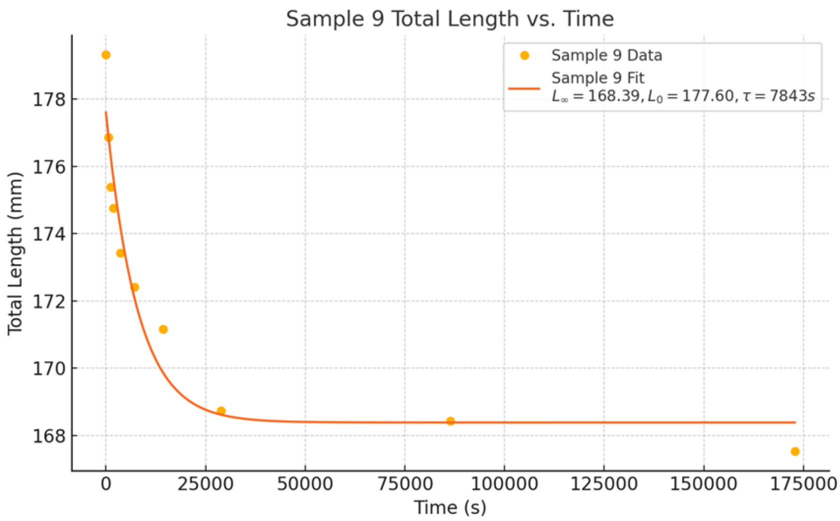

Figure 1. 17 Specimen 9 Total Length vs Relaxation Time

A similar observation was made for another specimen, which was subjected to tensile loading at a crosshead speed of 300 mm/min. The difference between the maximum extensometer elongation and crosshead displacement was 6.62 mm, compared to 10.9 mm in the quasi-static test. This indicates that under higher strain rates, deformation becomes more concentrated in the gauge section, whereas at lower strain rates, a greater portion of the deformation extends into the shoulder and grip regions. The corresponding length recovery over time is shown in Figure 1.18.

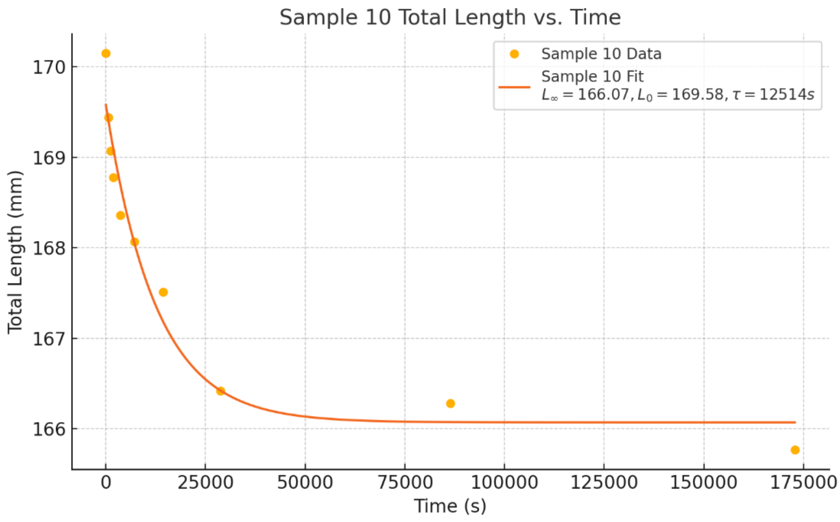

Figure 1. 18 Specimen 10 Total Length vs Relaxation Time

2 Constitutive Modelling

Recent studies have proposed various constitutive frameworks to characterize the mechanical behavior of tough photopolymers and thermoplastic elastomers. Saelen et al. [1] calibrated the Formlabs Durable V2 resin with a modified Bergström–Boyce (BB) model, in which the original strain-dependent flow law was replaced with a pressure-sensitive term, thereby improving the model's accuracy in simulating rate-dependent behavior. Shahin [5] applied the PolyUMod Three-Network Model (TN) to thermoplastic and thermoset polymers, successfully capturing their nonlinear viscoelastic response over a broad temperature range. Reis [3] extended the BB framework by incorporating a Mullins-type softening parameter to reproduce the cyclic softening behavior of polyurethane elastomers, using an Ogden-based elastic skeleton together with the Dorfmann–Ogden damage model. In a separate study, Almomani [6] introduced the TNV (Three-Network Viscoplastic) model, which combines Yeoh hyperelasticity with Mullins damage and plastic flow, and achieved high accuracy in reproducing both large-strain and hysteresis behavior of HDPE. In another approach, Qi [7] developed a physically motivated, phase-transition-based framework to account for the dual-phase behavior of amorphous polymers across the glass transition temperature; this was further extended by Liu et al. [8] to incorporate viscoelastic and viscoplastic elements for thermo-mechanical coupling. Mian et al. [16] calibrated PLA, ABS, and PETG using the BB, TN, and TNV models and conducted a comparative analysis. These works highlight the integration of hyperelasticity, viscoelasticity, rate sensitivity, and damage mechanisms in constitutive formulations.

Building upon these contributions, the present study selects four candidate constitutive models that integrate different levels of hyperelasticity, rate sensitivity, damage accumulation, hydrostatic pressure dependence and temperature dependence to evaluate the mechanical behavior of Anycubic Tough Resin Ultra.

(1) Ansys Bergstrom-Boyce Mullins model
(2) Ansys TN model
(3) Abaqus PRF 3 Network Yeoh Power-law Flow Mullins model
(4) PolyUMod TNV model

Given that the primary aim of the study was material model calibration, the experimental data mainly served for fitting and validation purposes. Therefore, although the number of replicate tests was limited, it was considered sufficient for capturing the essential mechanical characteristics required for modelling.

The material models are calibrated using MCalibration®, a calibration platform developed by Ansys that provides access to a broad range of built-in constitutive models and supports parameter optimization through integration with the PolyUMod® library. It incorporates multiple optimization algorithms, including genetic algorithms, the Nelder–Mead simplex method, and others. Additionally, it provides interfaces to various commercial finite element software packages, such as Ansys, Abaqus, enabling integration of calibrated material models into numerical simulations.

2.1. Complete Tensile Test Plan

Following the smart testing methodology proposed by Jorgen Bergstrom [9], a smart experiment plan was designed to efficiently extract a wide range of mechanical information from few specimens.

To calibrate the material models, a series of mechanical tests were first conducted at 23 °C, followed by additional tests at 5 °C, 35 °C, and 45 °C to evaluate the temperature dependence. The complete test matrix performed at room temperature (23 °C) is summarized in Table 2.1 as an example, the same tests were repeated under other temperatures using an environmental chamber (Figure 2.1) for extracting temperature dependent parameters.

Figure 2. 1 MTS Environmental Chamber

Table 2. 1 Complete Test Plan of 23℃

No.	Temp	Test
1	296 K	Quasi static tensile test at 3 mm/min, run to failure.
2	296 K	High strain rate tensile test at 300 mm/min, run to failure.
3	296 K	Cyclic Loading and unloading at 3 mm/min (1) Load to 2% strain, hold for 1 min, then unload to 0 stress. (2) Load to 5% strain, hold for 2 min, then unload to 0 stress. (3) Load to 10% strain, hold for 10 min, then unload to 0 stress. (4) Load to 20% strain, hold for 10 min, then unload to 0 stress. (5) Load to 40% strain, hold for 10 min, then unload to 0 stress. (6) Final loading to failure.
4	296 K	Cyclic Loading and unloading at 30 mm/min without holding (1) Load to 5% strain, then unload to 0 stress. (2) Load to 10% strain, then unload to 0 stress. (3) Load to 20% strain, then unload to 0 stress. (4) Load to 30% strain, then unload to 0 stress. (5) Load to 40% strain, then unload to 0 stress. (6) Final loading to failure.

2.2. Ansys Bergstrom-Boyce Mullins

In the Bergstrom-Boyce (BB) model the applied deformation gradient is acting on two parallel networks, see the following rheological representation (Figure 2.2).

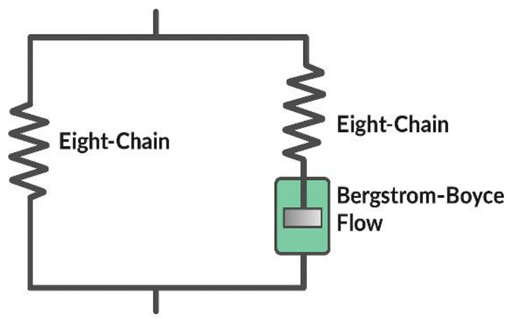

Figure 2. 2 Rheological model of Ansys BB Mullins

First, the time-stress-strain data under room temperature (23℃) was imported into MCalibration®, using the Ansys Bergstrom-Boyce Mullins model and Extensive Automatic optimization (Figure 2.3).

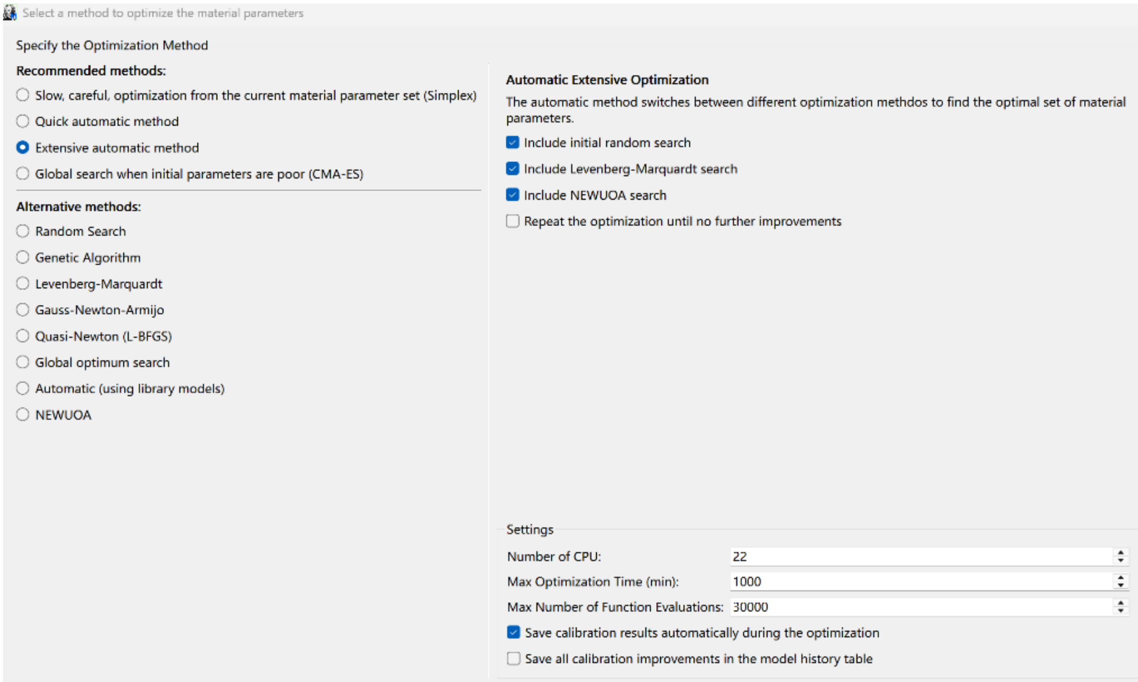

Figure 2. 3 MCalibration® Calibration Settings

The calibration result was plotted in Figure 2.4.

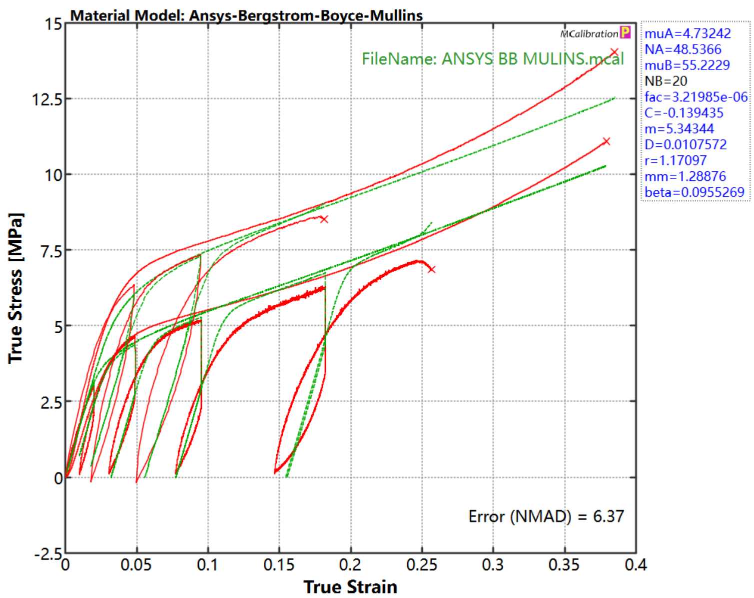

Figure 2. 4 MCalibration® Fitting Result

The two-network model is capable of capturing strain-rate dependence and nonlinear viscoelastic behaviour. Although the NMAD is relatively low, it fails to reproduce the hysteresis loops observed in cyclic loading, highlighting a key restriction of the two-network model. This suggests the necessity of extending the model to a three-network framework for improved accuracy.

2.3. Ansys TN Model

The Ansys TN (Three Network Model) is a non-linear viscoelastic material model for thermoplastics and thermosets. It consists of three networks, the structure is shown in Figure 2.5.

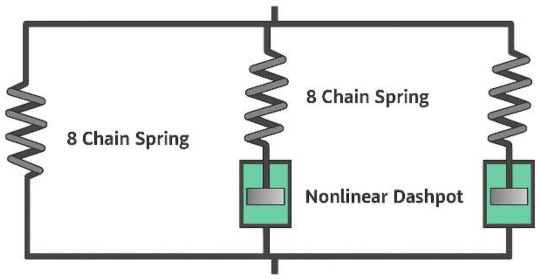

Figure 2. 5 Ansys TN Model

This model is capable of simultaneously fitting stress–strain curves across multiple temperatures, thanks to its built-in temperature-dependent formulations for both hyperelastic and flow behaviour. Specifically, one of the networks is a temperature-dependent Aruda–Boyce hyperelastic network, which captures the equilibrium (instantaneous) elastic response. The viscoelastic networks share the same elastic backbone but include a scaling factor to reflect time-dependent behaviour, and they are connected to two nonlinear dashpots with temperature dependent flow rule, enabling it to reproduce complex time–temperature responses.

Cauchy stress acting on networks A, B and C is given by a temperature-dependent version of the Aruda-Boyce eight-chain model:

$$\boldsymbol{\sigma}_n = \frac{\mu_n}{\boldsymbol{J}_e^{(n)} \lambda_e^{(n)*}} \left[1 + \frac{\theta - \theta_0}{\hat{\theta}}\right] \mathcal{L}^{-1}\left(\frac{\lambda_L}{1}\right) \mathcal{L}^{-1}\left(\frac{\lambda_L}{\lambda_e^{(n)*}}\right) dev\left(\boldsymbol{b}_e^{(n)*}\right) + \kappa\left(\boldsymbol{J}_e^{(n)} - 1\right)\boldsymbol{I} \quad (2.\ 1)$$

where:

$\boldsymbol{J}_e^{(n)} = det\left(\boldsymbol{F}_e^{(n)}\right).$

$\boldsymbol{b}_e^{(n)*} = \left(\boldsymbol{J}_e^{(n)}\right)^{-2/3} \boldsymbol{F}_e^{(n)} \left(\boldsymbol{F}_e^{(n)}\right)^T$ is the Cauchy-Green deformation tensor.

$\lambda_e^{(n)*} = \left(\frac{\mathrm{tr}\left(\boldsymbol{b}_e^{(n)*}\right)}{3}\right)^{1/2}$ is the effective chain stretch.

$L^{-1}(x)$ is the inverse Langevin function, where $L(x) = \coth(x) - \frac{1}{x}$.

The flow stress acting on network A and B is expressed as follows:

$$\dot{\gamma}_A = \dot{\gamma}_0 \cdot \left(\frac{\tau_A}{\widehat{\tau_A} + aR(p_A)}\right)^{m_A} \cdot \left(\frac{\theta}{\theta_0}\right)^{n} \quad (2.\ 2)$$

$$\dot{\gamma}_B = \dot{\gamma}_0 \cdot \left(\frac{\tau_B}{\widehat{\tau_B} + aR(p_B)}\right)^{m_B} \cdot \left(\frac{\theta}{\theta_0}\right)^{n} \quad (2.\ 3)$$

where:

$\dot{\gamma}_0 = 1/s$ is a constant introduced for dimensional consistency.

p_A *and* p_B is hydrostatic pressure.

$R(x) = \frac{x+|x|}{2}$ is the ramp function.

$\widehat{\tau_A}$, a, m_A, n are specified material parameters.

As it shows in Equation 2.1, 2.2 and 2.3, the influence of temperature is integrated to the equations, either by linear dependence (2.1) or exponential term (2.2 and 2.3).

Figure 2.6 shows the calibration result across different temperatures. Although the overall fitting error (NMAD = 11.5) is acceptable, several discrepancies are observed.

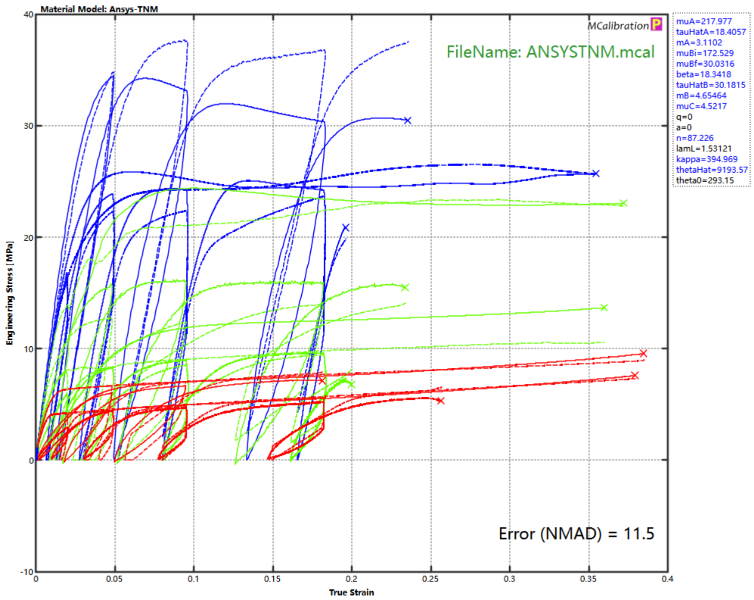

Figure 2. 6 Ansys TN calibration result

At low temperatures (Figure 2.7), the model significantly overestimates the peak stresses and underpredicts energy dissipation during unloading, resulting in narrow hysteresis loops.

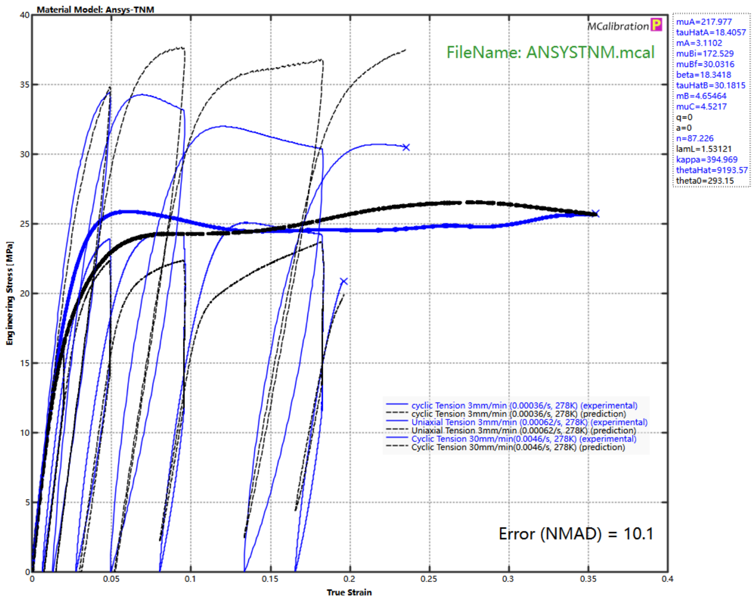

Figure 2. 7 Ansys TN calibration result in 278K

At high temperatures (Figure 2.8), the initial stiffness is noticeably overestimated, suggesting insufficient thermal softening in the equilibrium response.

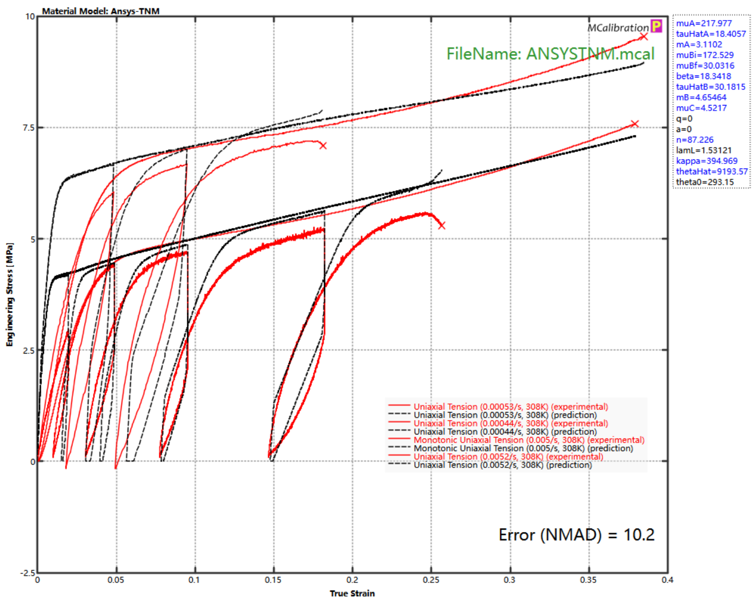

Figure 2. 8 Ansys TN calibration result in 308K

Despite these issues, the residual strains at the end of each cycle are well captured, indicating that the viscoelastic network's flow response is effective. It is also worth noting that some of the discrepancies, particularly under low-temperature and high strain rate conditions, may partially stem from increased noise levels in the experimental data, which inherently limits the achievable accuracy of the model fitting. Conclusively, the Ansys TN model provides a usable, though not highly precise, prediction of the experimental data across a wide temperature range.

2.4. Abaqus PRF 3N Yeoh Mullins Power-law Flow

The PRF-3YP model is a native model in Abaqus, it is a special case of the general Parallel Rheological Framework (PRF) models. The structure of the PRF-3N-Yeoh-Powerlaw model was selected in order to get a relatively simple parallel network structure that is suitable for some elastomer materials.

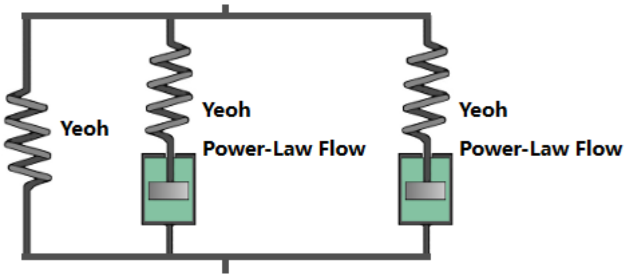

Figure 2. 9 Abaqus PRF 3N Yeoh Powerlaw Flow

The Abaqus PRF 3YP model is a predefined three-yield-point plasticity model primarily designed to capture nonlinear elastic–plastic behaviour. However, it does not account for temperature dependence or time-dependent effects such as viscoelasticity. Therefore, separate calibrations were performed at each temperature, and the results were combined using the built-in Abaqus temperature interpolation scheme. Figure 2.10 presents the fit at 308 K as a representative case. Although the model achieves a relatively low NMAD at this temperature, it fails to capture key features of the material response under cyclic loading. In particular, it significantly underestimates hysteresis and cannot reproduce the sharp transitions during unloading and reloading at high strain rates. Since the model predominantly reflects hyperelastic and plastic behaviour without time-dependent dissipation, further calibration at other temperatures was deemed unnecessary.

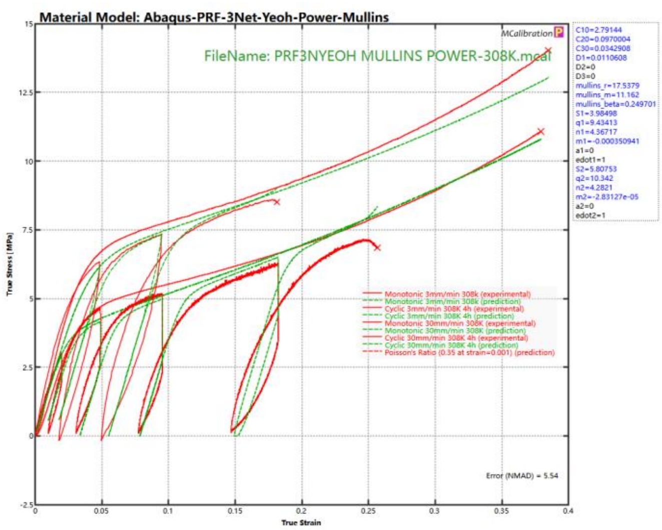

Figure 2. 10 Abaqus PRF 3N Yeoh Powerlaw calibration result

2.5. PolyUMod TNV Mullins model

Saelen [2] investigated the mechanical properties of Formlabs Durable V2 resin and found that its elastic behaviour is comparable to that of high-density polyethylene (HDPE) and polypropylene (PP). Almomani [6] successfully calibrated HDPE using the PolyUMod TNV model, capturing both strain rate, hydrostatic pressure and temperature-dependent characteristics. Mian et al. [16] calibrated PETG by TNV model both in compression and tension. Inspired by these studies, the present work explores the application of the PolyUMod TNV model to Anycubic Tough Resin Ultra, aiming to assess its capability in capturing the material's complex viscoelastic behaviour across different strain rates and temperatures. Figure 2.11 shows the structure of PolyUMod TNV model employed in this work.

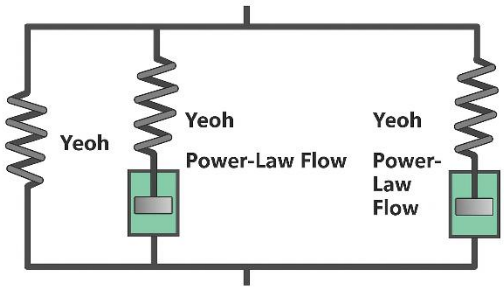

Figure 2. 11 PolyUMod TNV Rheological model

Network 1 is modeled as a purely hyper-elastic branch using the Yeoh strain energy function with Mullins Effect, capturing the nonlinear elastic response under small to moderate deformations. Networks 2 and 3 are defined as Neo-Hookean (1st order Yeoh spring) elastic components in parallel with nonlinear dashpots governed by power-law flow rules. The Mullins damage is confined to Network 1 (hyperelastic), while Networks 2 and 3 are defined as hyperelastic plus power-law viscoplastic flow components. This configuration allows the model to represent both rate-dependent (viscoplastic) and temperature behaviors under large deformation.

The total deformation gradient F acts on all three networks:

$$\boldsymbol{F} = \boldsymbol{F_a} = \boldsymbol{F_b} = \boldsymbol{F_c} \quad (2.\ 4)$$

The total stress is the sum of the contributions from all three networks:

$$\boldsymbol{\sigma} = \boldsymbol{\sigma}^{(A)} + \boldsymbol{\sigma}^{(B)} + \boldsymbol{\sigma}^{(C)} \quad (2.\ 5)$$

The viscoelastic deformation gradient acting on each network is decomposed into elastic and viscoplastic parts:

$$\boldsymbol{F} = \boldsymbol{F}^e \boldsymbol{F}^v \quad (2.\ 6)$$

The Cauchy stress acting on a network is given by the Yeoh model with Cauchy stress:

$$\boldsymbol{\sigma} = \frac{2f_{\varepsilon}\eta}{J^e}(C_{10} + 2C_{20}(\boldsymbol{I}_1^* - 3) + 3C_{30}(\boldsymbol{I}_1^* - 3)^2)\mathrm{dev}[\boldsymbol{b}^*]$$

$$+(\kappa_1(J^e - 1) + \kappa_2(J^e - 1)^3 + \kappa_3(J^e - 1)^5)\boldsymbol{I} \quad (2.7)$$

Where $\boldsymbol{\sigma}$ is the Cauchy stress, f_ε is the plastic flow evolution damage factors, $C_{10}, C_{20,} C_{30}$ are the Yeoh model parameters, J^e is the determinant of the elastic deformation gradient, η is the Mullins damage factor, $\boldsymbol{b}^*$ is the left Cauchy-Green deformation tensor, $\boldsymbol{I}$ is the first principal invariant of the Cauchy tensor, and κ_1 κ_2 κ_3 are the bulk moduli. The Mullins damage factor η is given by:

$$\eta_A = 1 - \frac{1}{r}\,\mathrm{erf}\left(\frac{U_{\mathrm{dev}}^{\max A} - U_{\mathrm{dev}}^{A}}{\hat{U} + \beta U_{\mathrm{dev}}^{\max A}}\right) \quad (2.8)$$

Where r $\hat{U}$ β are material parameters. The variable U_{dev}^{A} is the current deviatoric strain energy density in network A, and $U_{\mathrm{dev}}^{\max A}$ is the max deviatoric strain energy density that network A has been exposed to. The Mullins damage calculation is deactivated if $r = 0$. The plastic flow evolution damage factor $f_{\varepsilon A}$ is given by the differential equation:

$$\frac{df_{\varepsilon A}}{dt} = \frac{1}{c_\varepsilon}(f_s - f_{\varepsilon A})\dot{\gamma}_A \quad (2.9)$$

Here, f_s c_ε are material parameters, $f_{\varepsilon A} = 1$ at t = 0 and $\dot{\gamma}_A$ is a constantintroduced for dimensional consistency. The velocity gradient of the viscoplastic flow of network A can be written as:

$$\dot{F}_A^v = \dot{\gamma}_0\left[R\left(\frac{\tau_A}{f_p \cdot f_{\varepsilon p} \cdot \hat{\tau}_A} - 0.001\right)\right]^m F_A^{e^{-1}}\left[N_A + b\,\mathrm{sign}(\mathrm{tr}(\boldsymbol{\sigma}))I\right]F \quad (2.10)$$

where $\hat{\tau}_A$ m are material parameters. $\dot{\gamma}_0 = 1/s$ is a constant introduced for dimensional consistency. $R(x) = \frac{x+|x|}{2}$ is the ramp function, $\hat{\tau}_A$ is the flow resistance of the network, m is a stress exponent, f_p is a pressure dependent viscoplastic flow, N_A is the tensor that specifies the direction of the driving deviatoric stress and the term $b\,\mathrm{sign}(\mathrm{tr}(\sigma))I$ gives the volumetric viscoplastic flow, where b is a material parameter. The effective stress driving the viscoplastic flow is given by the Hill deviatoric stress:

- $\tau_A = [F(\sigma_{A.22} - \sigma_{A.33})^2 + G(\sigma_{A.33} - \sigma_{A.11})^2 + H(\sigma_{A.11} - \sigma_{A.22})^2 + 2L\sigma_{A.23}^2 + 2L\sigma_{A.31}^2 + 2L\sigma_{A.12}^2)]^{1/2}$ (2. 11)

If the parameter $F = 0$, then the model yields isotropy and the effective stress is instead given by the square of the Frobenius norm of the deviatoric stress:

$$\tau_A = \left[\sum_{i=1}^{3}\sum_{j=1}^{3}\left|\sigma_{A.ij}\right|^2\right] \quad (2.12)$$

In these equations, $\boldsymbol{\sigma} = \mathrm{dev}[\boldsymbol{\sigma}_A]$ represents the deviatoric stress. The tensor $\boldsymbol{N_A}$ specifies the direction of the driving deviatoric stress of the relaxed configuration converted to the current configuration:

$$N_A = \frac{dev[\boldsymbol{\sigma}_A]}{\tau_A} \quad (2.13)$$

The pressure dependence of viscoplastic flow in the TNV model is introduced through a scaling function that modifies the flow resistance based on the hydrostatic pressure: If $p_0 > 0, f_p = \max\left(0.5,\ 1 + \frac{p_0 p}{\tau_A}\right)$; If $p_0 < 0$ and $p < 0, f_p = \max\left(0.5,\ 1 - \frac{p_0 p}{\tau_A}\right)$; $f_p = 1$, *otherwise*. $p = -\frac{1}{3}\,\mathrm{tr}(\boldsymbol{\sigma_A} + \boldsymbol{\sigma_B} + \boldsymbol{\sigma_C})$ is the hydrostatic pressure. Summarily, if $p_0 > 0$, then the yield stress is reduced in a tensile pressure state and increased in a compressive pressure state. If $p_0 < 0$, then the yield stress is only reduced in a tensile pressure state.

2.5.1. Parameter Identification

The tensile calibration results in 278 K, 296 K, 308K and 318K are depicted in Figure 2.12(a), Figure 2.12(b), Figure 2.12(c) and Figure 2.12(d)

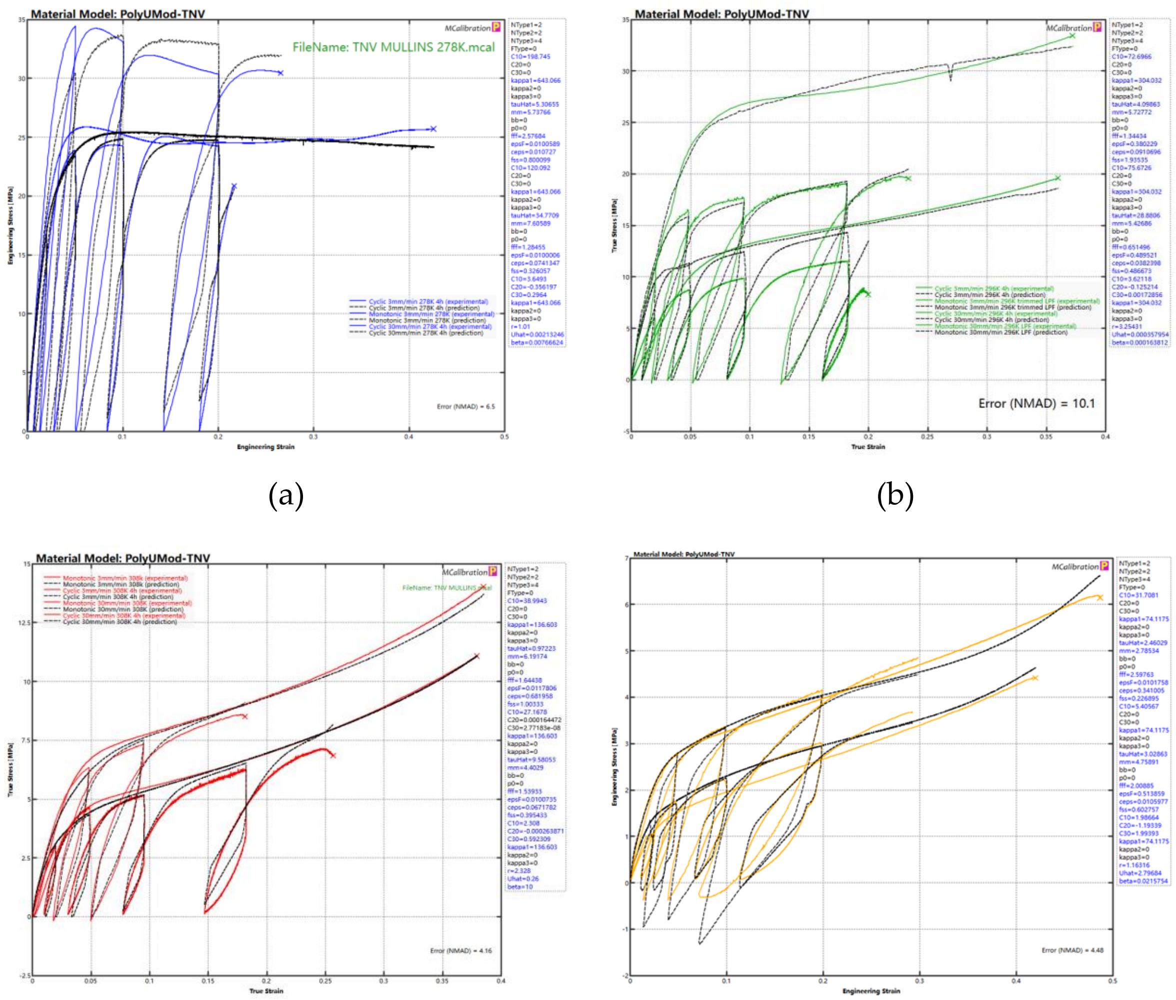

(a) (b) (c) (d)

Figure 2. 12 PolyUMod TNV calibration

The Three-Network Viscoplastic (TNV) model presented here shows high predictive accuracy across the experimental strain range, particularly in capturing the hysteresis loops of cyclic behavior. As illustrated in the fitting results, the normalized mean absolute deviation (NMAD) remains very low across all the four datasets, despite slight deviation in the 2nd and 4th group due to inherent experimental uncertainties. Notably, the TNV model with Mullins effect embedded in the hyperelastic network successfully reproduces the hysteresis loops during unloading–reloading cycles, as well as residual strain after each unloading phase. The residual strain at the end of each cycle is accurately predicted by the model without additional tuning, indicating that the flow damage parameters (e.g. epfs, ceps, fss, fff) are well calibrated. Strain hardening in the final stages of loading is also well captured, showing consistency with the permanent network extension under large deformation. The material parameters under each temperature are listed in Table 2.2.

Table 2. 2 PolyUMod Material Model Parameters

	278K	296K	308K	318K	Network
C10	192.84	81.65	47.36	31.71	1
kappa1	639.17	311.8	122.98	74.12	1
tauHat	5.89	4.93	4.85	2.46	1
mm	6.25	4.97	3.92	2.79	1
fff	2.47	1.28	2.63	2.6	1
epsF	0.0107	0.0178	0.9386	0.0102	1
ceps	0.0102	0.1424	0.1348	0.341	1
fss	0.694	1.0154	0.843	0.2269	1
C10	121.06	71.89	16.28	5.41	2
kappa1	628.54	311.8	122.98	74.12	2
tauHat	36.39	22.43	9	3.03	2
mm	8.45	6.11	5.15	4.76	2
fff	1.06	1.1	2	2.01	2
epsF	0.01	0.0102	2.4997	0.5139	2

ceps	0.0537	0.0546	0.1371	0.0106	2
fss	0.2914	0.6104	0.8122	0.6028	2
C10	3.34	2.93	2.23	1.99	3
C20	-0.2126	-0.1768	0.2501	-1.1934	3
C30	1.5098	0.0037	0.1672	1.9939	3
kappa1	633.6	311.8	122.98	74.12	3
r	1.0119	2.4065	2.0639	1.1632	3
Uhat	0.0006	0.6281	0.0846	2.7968	3
beta	0.0109	0.01	0.0149	0.0216	3

As shown in Figure 2.12, the PolyUMod TNV model provides the most accurate tensile data fitting at each temperature, among all the evaluated models. Based on this result, we chose to further calibrate the TNV model against compression experiments in order to optimize the pressure-dependence parameter p_0 of Network 1 and Network 2, which governs the asymmetry between tensile and compressive stress–strain behavior. This strategy also reduces computational cost, as the other models showed poor agreement in tension and were therefore not pursued further for compression calibration. The complete compression test plan is listed in Table 2.3.

Table 2. 3 Compression Test Plan

No.	Temp	Test
1	278 K	Quasi static compression test at 1.3 mm/min, run to failure.
2	278 K	Dynamic compression test at 30 mm/min, run to failure.
3	296 K	Quasi static compression test at 1.3 mm/min, run to failure
4	296 K	Dynamic compression test at 30 mm/min, run to failure
5	318 K	(1) Quasi static compression test at 1.3 mm/min. (2) Stress relaxation for 600 seconds.
6	318 K	(1) Dynamic compression test at 30 mm/min to 30% engineering strain. (2) Unloading to 0 stress at same speed.

The compression experiment results of each temperature are shown in Figure 2.13.

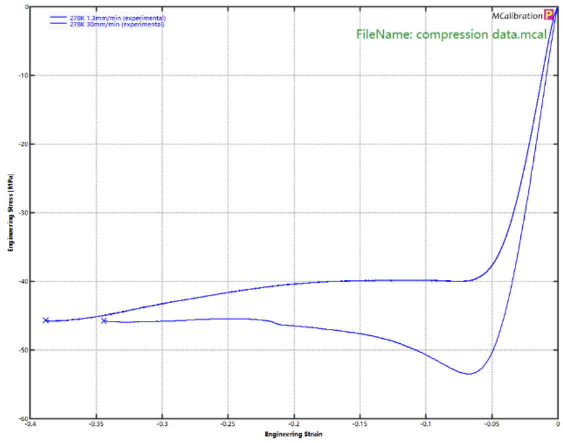

(a)

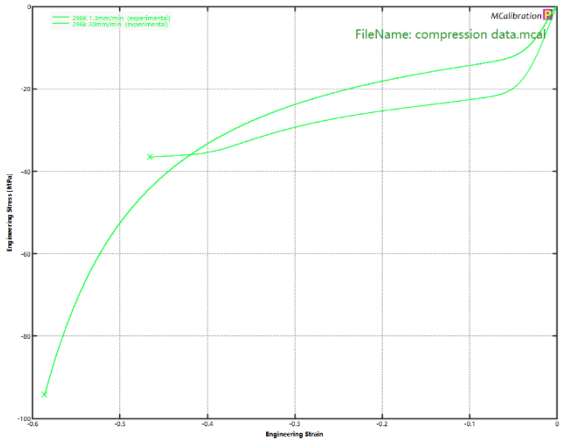

(b)

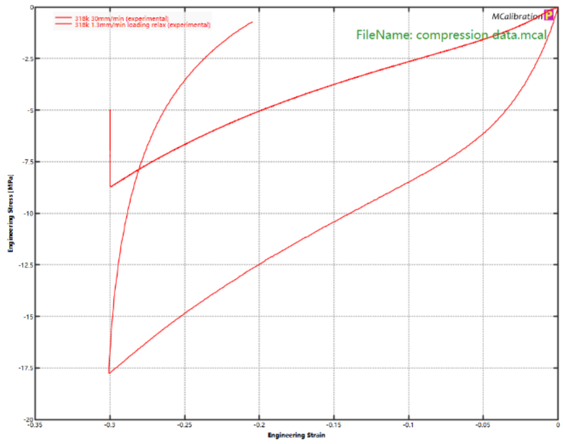

(c)

Figure 2. 13 Compression Test

We observe that at higher strain rates, both the initial stiffness and yield stress increase. However, the UTS at 278 K under 1.3 mm/min and 30 mm/min remains similar, likely due to self-heating effects. Owing to the cylindrical geometry of the compression specimen, heat dissipation is significantly slower than in thin dog bone shaped specimens. At room temperature (296 K), softening becomes apparent at around 0.4 strain, the flow stress doesn't rise while further compressing the specimen. When the temperature is elevated to 318 K, the material exhibits an almost linear response even under quasi-static loading, indicating that it has approached rubbery state.

This temperature-dependent behaviour is attributed to changes in the material's viscoelastic response: at lower temperatures, the polymer remains in a glassy or sub-glassy state, where internal damping from relaxation processes leads to greater energy dissipation and heat generation. In contrast, at elevated temperatures, increased molecular mobility and faster stress relaxation reduce energy dissipation.

To ensure reliable calibration, only quasi-static compression data were used to determine p_0, as self-heating becomes non-negligible under high-speed loading. The calibration results used to identify p_0 are shown in Figure 2.14.

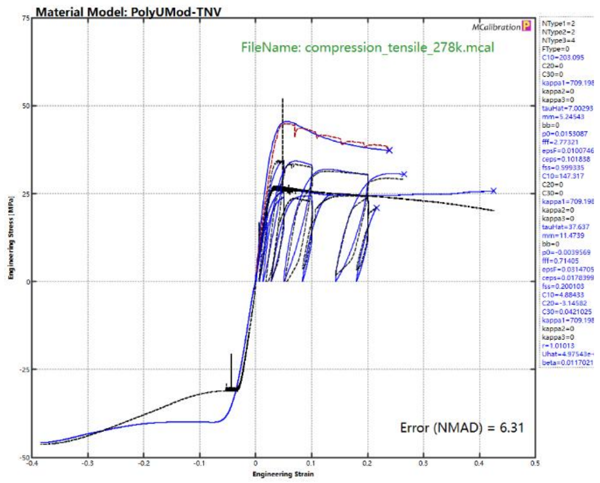

(a) 278K

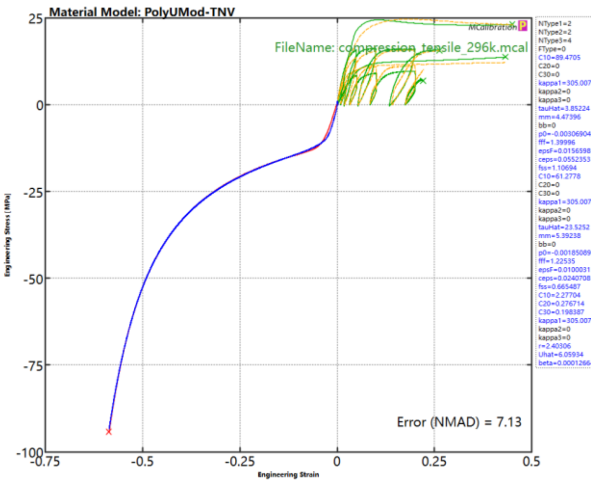

(b) 296K

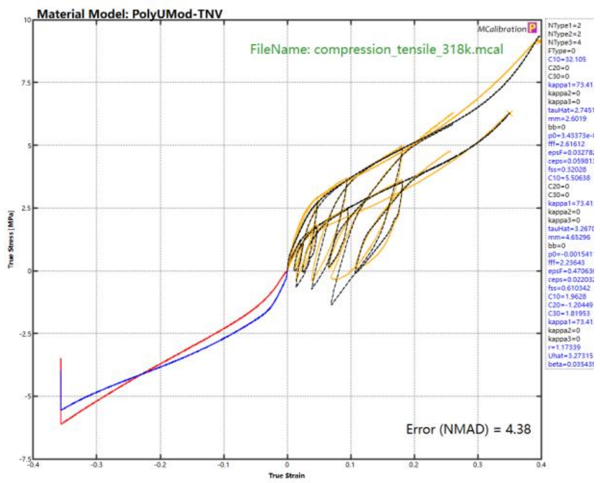

(c) 318K

Figure 2. 14 Calibration of pressure dependence p_0

The calibration results show that by introducing the pressure-dependence parameter p_0, the material model is able to capture the tension-compression asymmetry at 296 K and 318 K. While the model predicts the initial slope and ultimate compressive strength at 278 K reasonably well, it underestimates the yield stress under compression at this temperature.

2.5.2. Parametric Study

As shown in Figure 1.11(a) and Figure 1.11(b), both the Young's modulus and ultimate tensile strength exhibit a quasi-linear dependence on temperature. This observation suggests that the material parameters governing the stress–strain response—hereafter referred to as constructive parameters—should also follow a quasi-linear trend with temperature. In contrast, other parameters included in the model exert limited influence on the fitting results, as they are likely associated with plateau regions or flat minima in the cost function. For example, the bulk modulus Kappa1 varies substantially with temperature, decreasing from 633.6 to 74.12 as the temperature increases from 278 K to 318 K. However, the parametric study performed by varying its value across this full range while keeping all other parameters fixed, showed virtually identical stress–strain curves (Figure 2.15), this indicates that Kappa1 has minimal influence on the model's predictive accuracy.

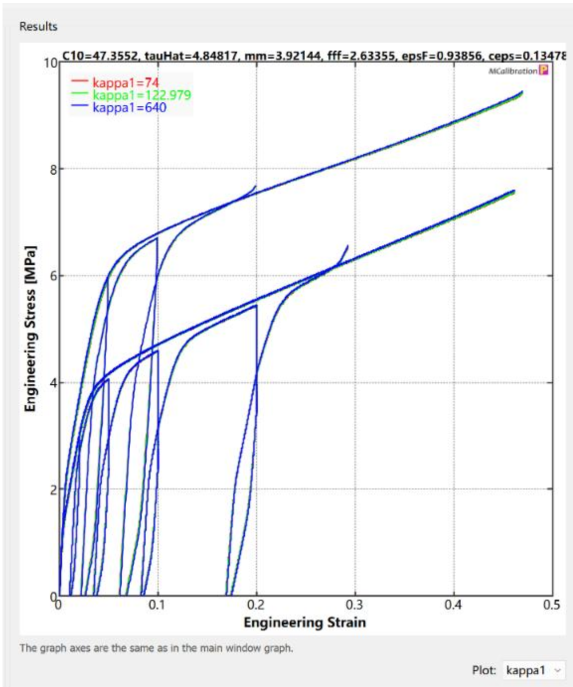

Figure 2. 15 Kappa1 parametric study result

As these structural parameters are intrinsic to the model formulation and not affected by temperature, sensitivity analysis was conducted at 308 K, and the identified parameters were consistently used for all temperatures.

Referring to Table 2.2, C10_1 decreases from 192 to 31 as the temperature increases from 278 K to 318 K. Its influence on the stress–strain response and the NMAD is illustrated in Figure 2.16.

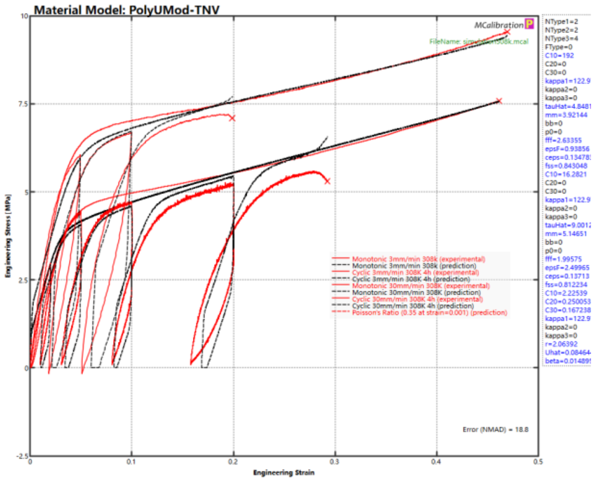

(a)

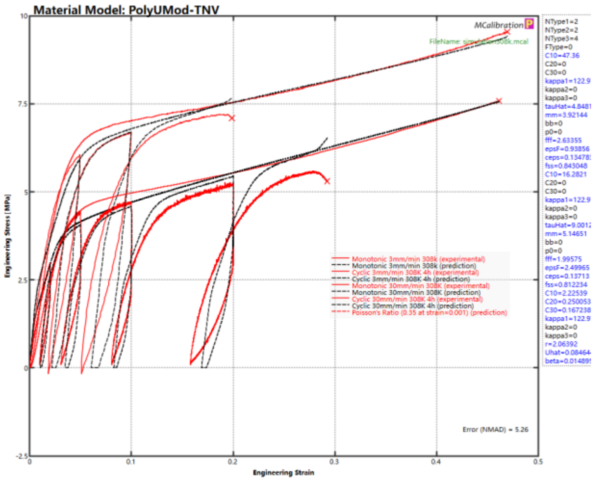

(b)

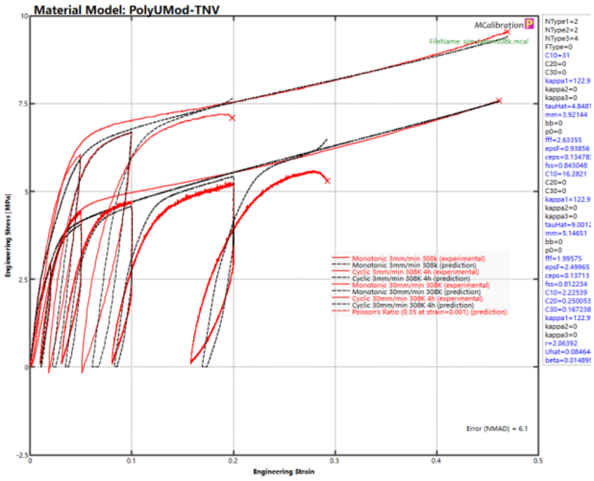

(c)

Figure 2. 16 C10_1 parametric study

As illustrated, both the curve shape and NMAD are influenced significantly, suggesting C10_1 is a structurally important parameter.

Similar studies were performed to the other parameters and the results are shown from Figure 2.17 to Figure 2.19.

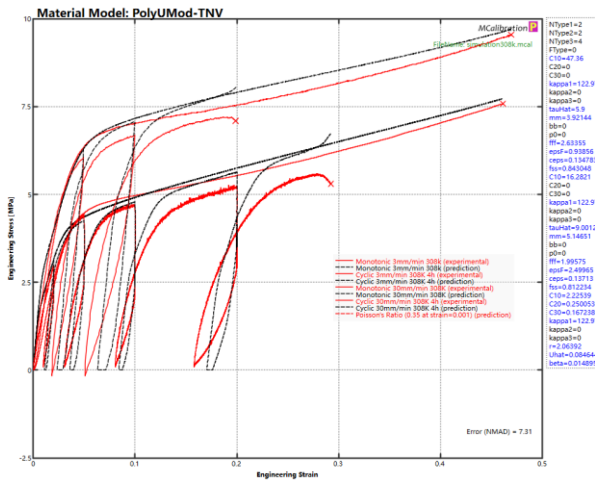

(a)

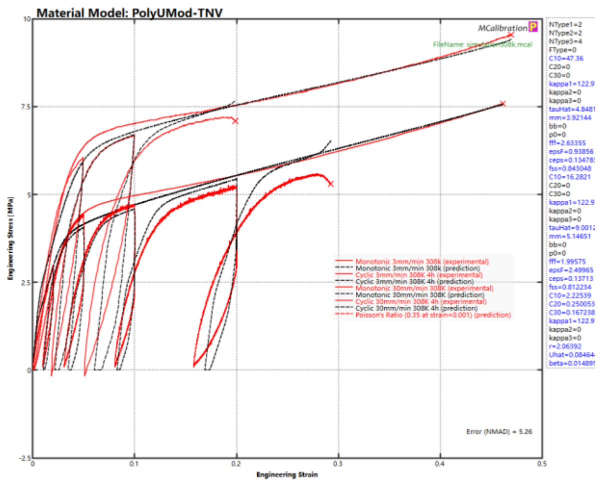

(b)

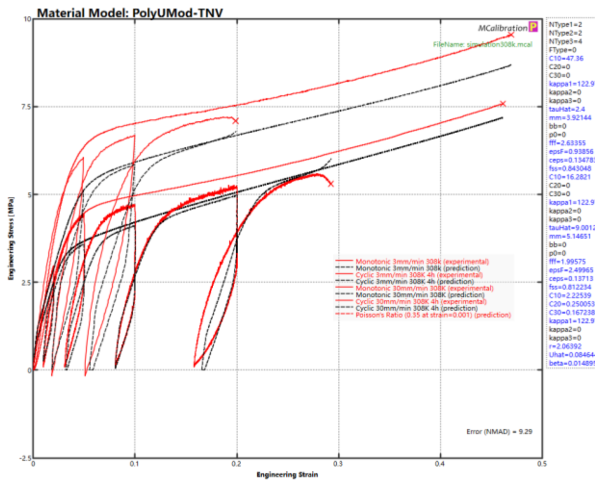

(c)

Figure 2. 17 tauHat_1 parametric study

As shown in Figure 2.17, while tauHat_1 taking the upper limit 5.9 or lower limit 2.4, the NMAD is 7.31 or 9.29 respectively, thus mm_1 is a parameter can affect the fitting result significantly.

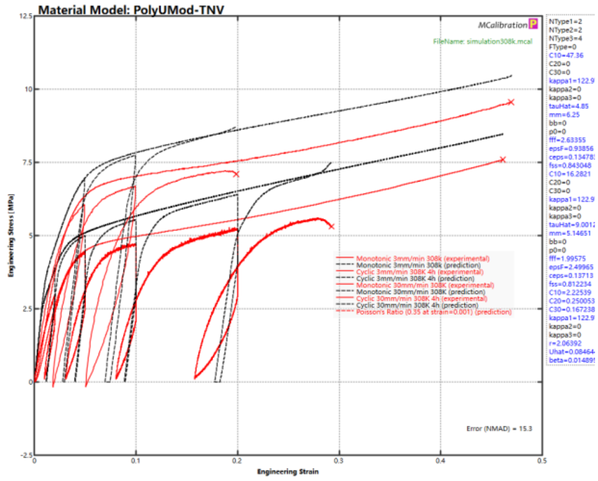

(a)

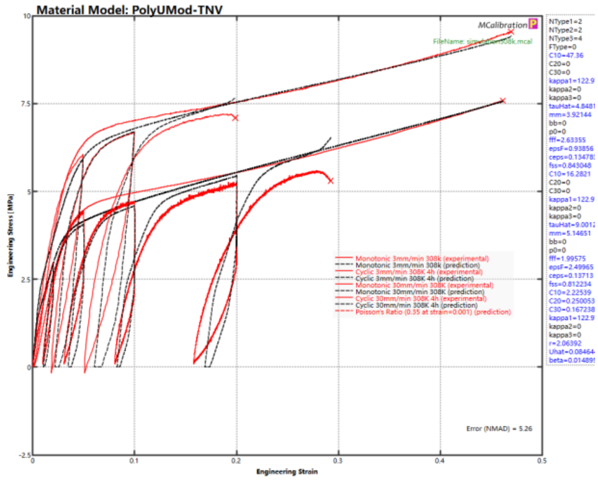

(b)

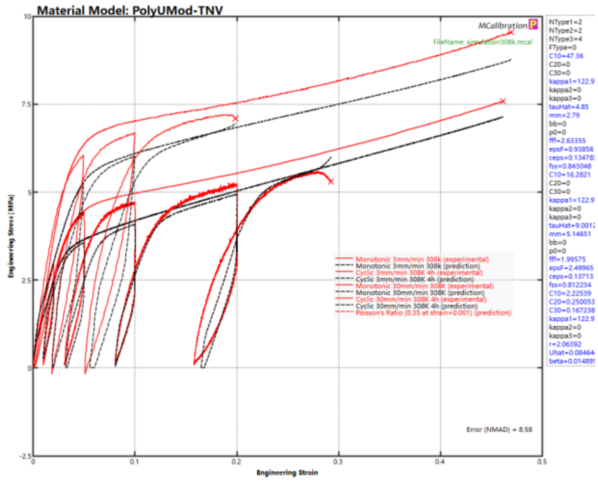

(c)

Figure 2. 18 mm_1 parametric study

As shown in Figure 2.18, while mm_1 taking the upper limit 6.25 or lower limit 2.79, the NMAD is 15.3 or 8.58 respectively, thus mm_1 is a parameter can significantly affect the fitting result.

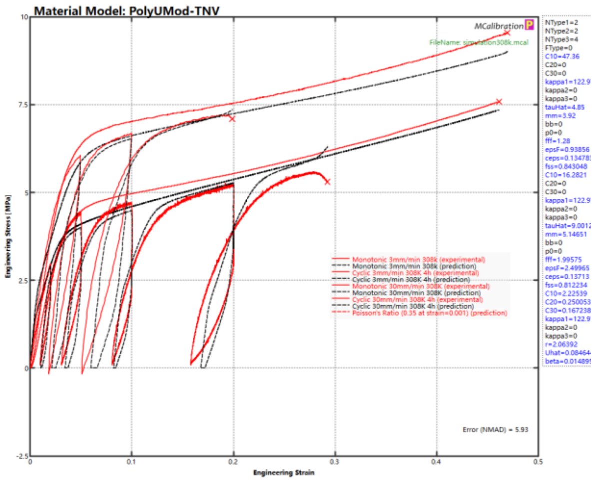

(a)

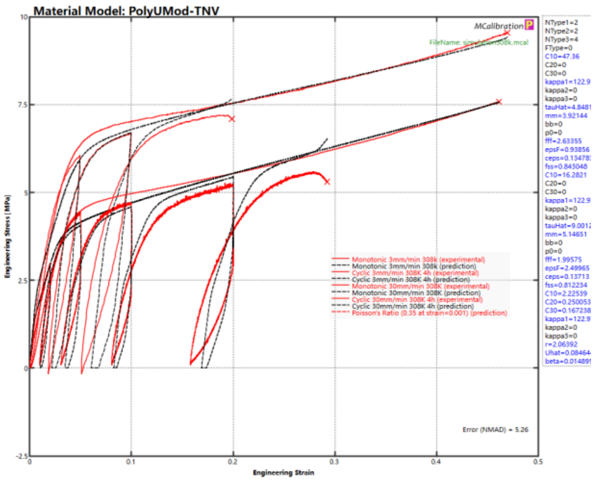

(b)

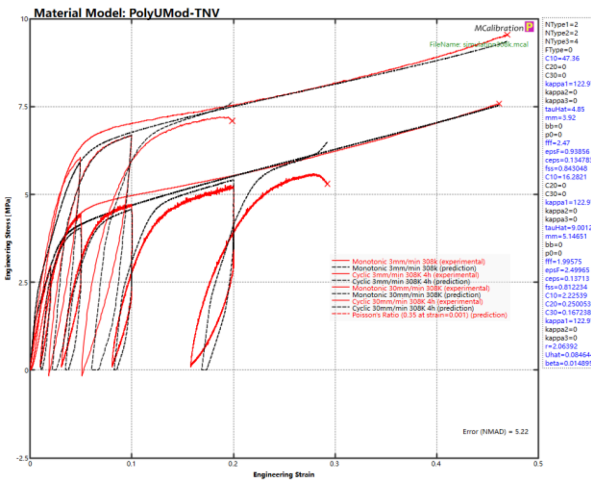

(c)

Figure 2. 19 fff_1 parametric study

As Figure 2.19 shown, fff_1 can affect the NMAD, but the influence is limited, we can neglect its influence while interpolating parameters according to temperature. Parameter epsF_1, ceps_1 and fss_1 were analyzed using the same approach. The results indicate that their influence on fitting accuracy and the stress–strain curve shape is negligible.

The same parametric studies were conducted to Network 2 and Network 3 parameters, the structural parameters that significantly affect the stress strain relation or NMAD are listed in Table 2.5

Table 2. 5 Constructive Parameters of TNV model

	278K	296K	308K	318K	Network
C10_1	192.84	89.5	47.36	32.1	1
tauHat_1	5.89	4.93	4.85	2.46	1
mm_1	6.25	4.97	3.92	2.79	1
C10_2	121.06	61.8	16.28	5.5	2
tauHat_2	36.39	23.52	9	3.26	2
mm_2	8.45	6.11	5.15	4.76	2
C10_3	3.34	2.93	2.23	1.96	3

The parameters in Table 2.5 were plotted according to temperature respectively.

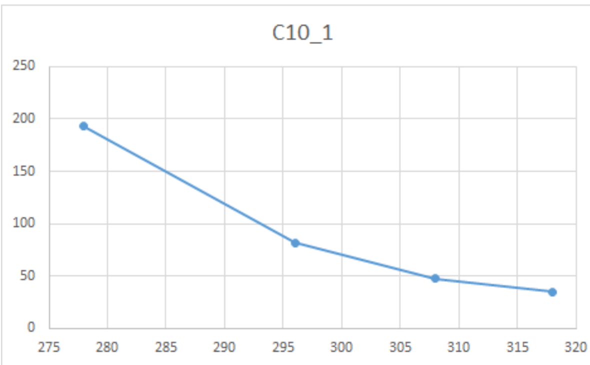

(Network 1)

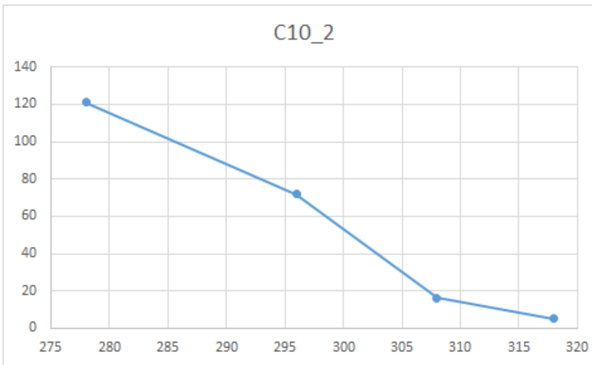

(Network 2)

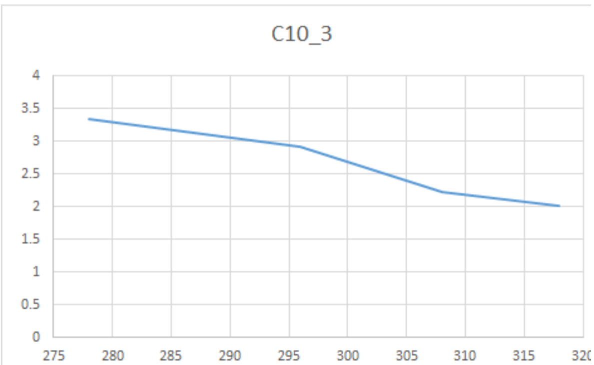

(Network 3)

Figure 2. 20 C10 of each network vs Temperature

It can be observed that C10 of each network decreases with increasing temperature with a quasi linear trend. As for parameter tauHat1 and tauHat2, it decreases with temperature. Although tauHat_1 value at 308K deviates from the trendline, the effect to NMAD and stress strain curve is negligible.

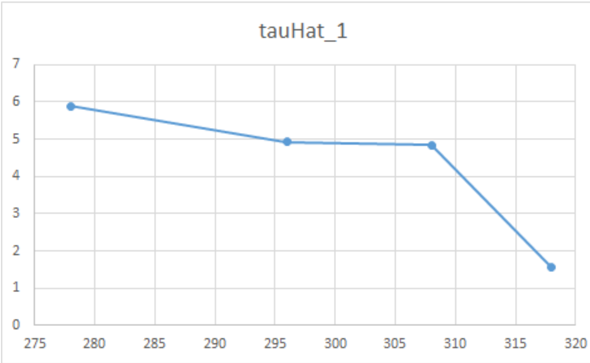

(Network 1)

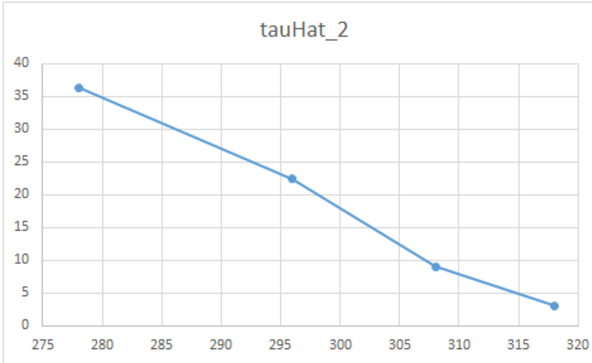

(Network 2)

Figure 2. 21 tauHat vs Temperature

Parameter mm of each network are plotted according to temperature in Figure 2.22, the trend is quasi linear as well.

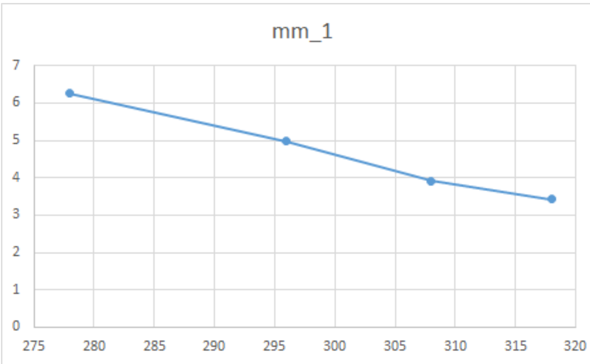

(Network 1)

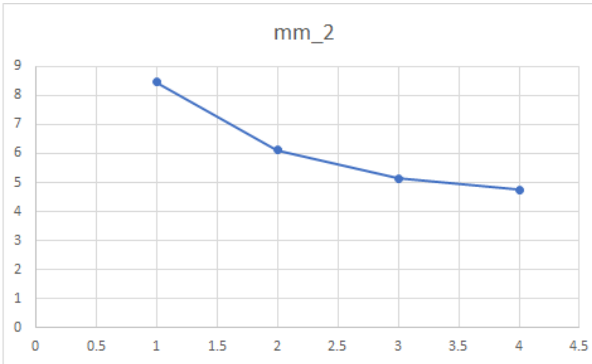

(Network 2)

Figure 2. 22 mm vs temperature

According to previous observations, the constructive material parameters show a quasi-linear relation to temperature, which is consistent to the trend of initial stiffness and UTS. The other parameters, although not linearly decreasing with temperature, show less influence on the fitting results. Therefore, linear interpolation can be applied to estimate these parameters and construct material models at intermediate temperatures between 5 °C and 45 °C. Temperatures above 45 °C were not tested, as the heat deflection temperature (HDT) lies between 50 °C and 55 °C [10]. Beyond 55 °C, the resin gradually transitions into a rubbery phase, becoming significantly softer and more ductile, and thus no longer operates in the glassy-state regime.

2.5.3. Multi Temperature Interpolation

Based on the conclusion in Section 2.5.2, the material models at each test temperature were integrated using the PolyUMod multi-temperature framework, which linearly interpolates material parameters as a function of temperature. The TNV model of each temperature are combined by Multi-Temperature frame of MCalibration®, the overall NMAD is 7.46, the calibration result is shown in Figure 2.23.

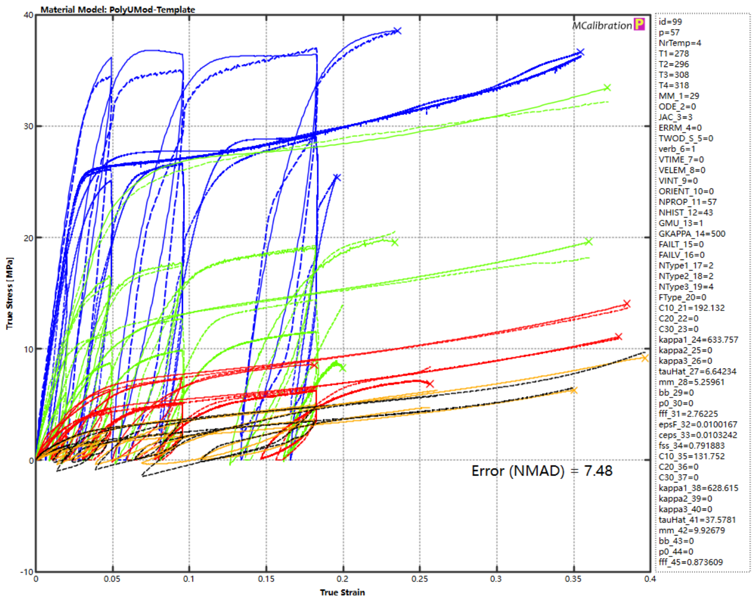

Figure 2. 23 TNV Multi Temperature Model

3 Numerical Model

3.1. Numerical Model Setup

The PolyUMod TNV Mullins material model was exported in LS-DYNA format. The resulting material card was then imported into ANSYS Workbench and solved using the LS-DYNA solver, which operates as a dynamic explicit solver.

To simulate the tensile test, a prescribed displacement history, identical to that used in the previous cyclic test at 278K, was applied to the upper grip (Figure 3.1(a)). The lower grip was constrained with fixed boundary conditions (Figure 3.1(b)).

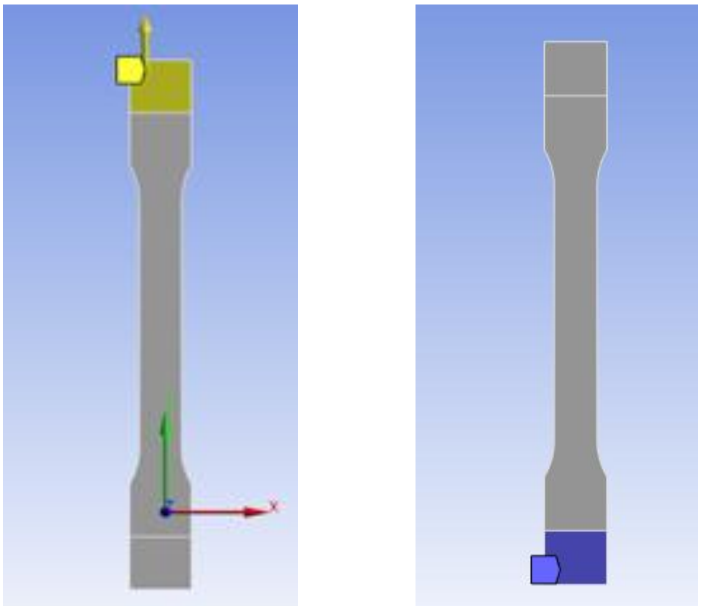

(a) (b)

Figure 3. 1 LS-DYNA Boundary Conditions

The displacement time history showed in Figure 3.2 is the same as the experiment.

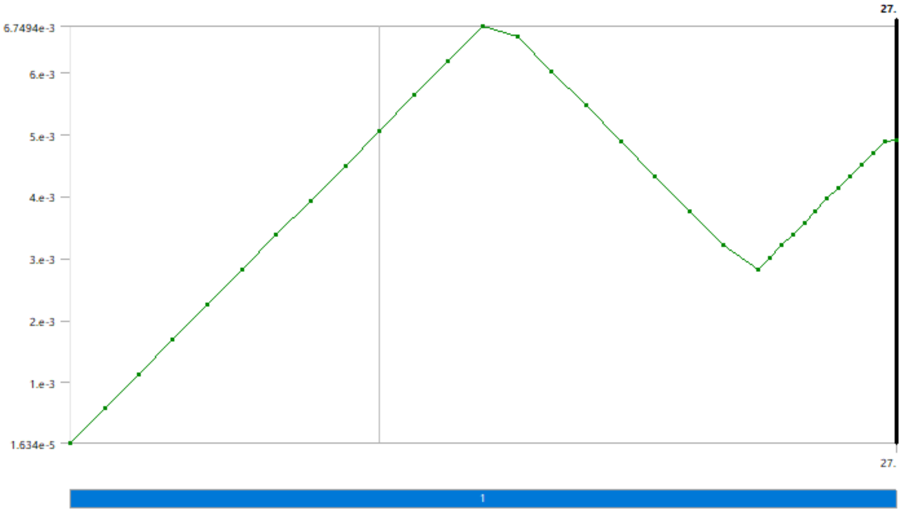

Figure 3. 2 Displacement history of loading grip

The extensometer was simulated by two reference points on the gauge section with a distance of 50 mm (Figure 3.3(a)), the axial deformation of the specimen was plotted in Figure 3.3 (b).

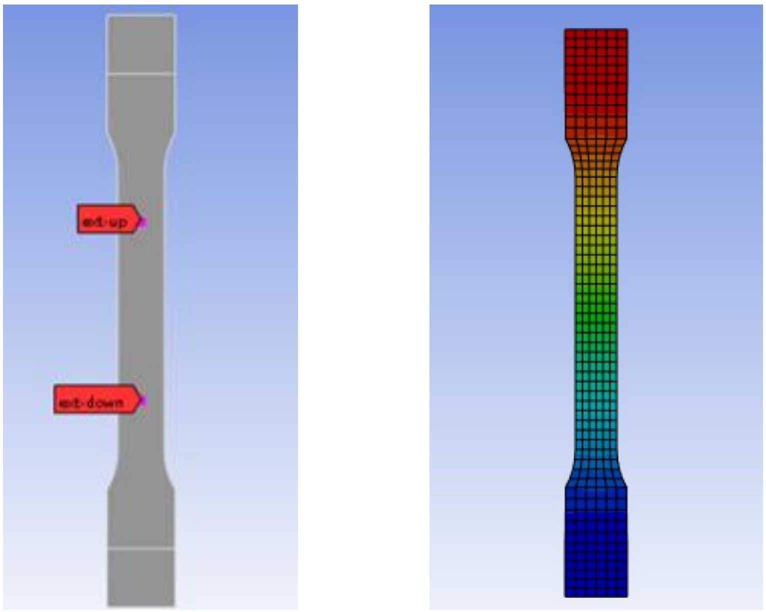

(b) (b)

Figure 3. 3 Extensometer Simulation

The first simulation was performed at 278K using an element size of 0.5 mm to ensure high accuracy. Subsequently, the same simulation was repeated with an element size of 3 mm. The results (Figure 3.4) show negligible differences between the medium and fine meshes, indicating that the solution is mesh-independent. Therefore, the 3mm element size was selected for subsequent simulations to balance computational cost and accuracy.

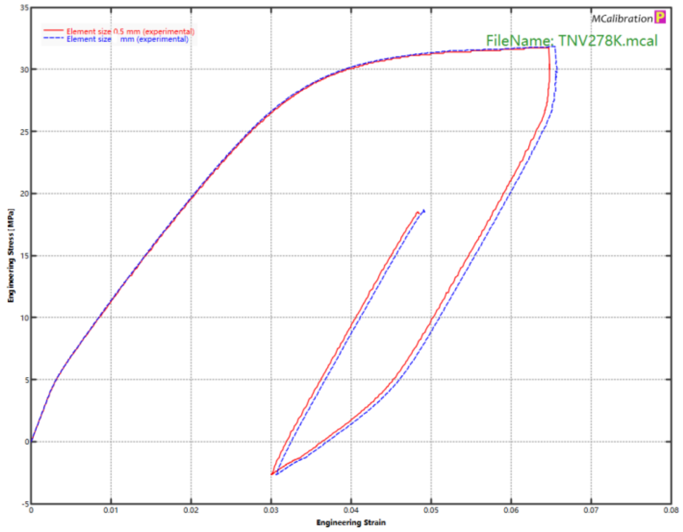

Figure 3. 4 TNV Mullins 278K Mesh Sensitivity

3.2. Cyclic Loading Validation

To further validate the material model, a cyclic loading test with exactly same displacement history of cyclic loading test in 278K. The displacement history of loading grip is showed in Figure 3.5.

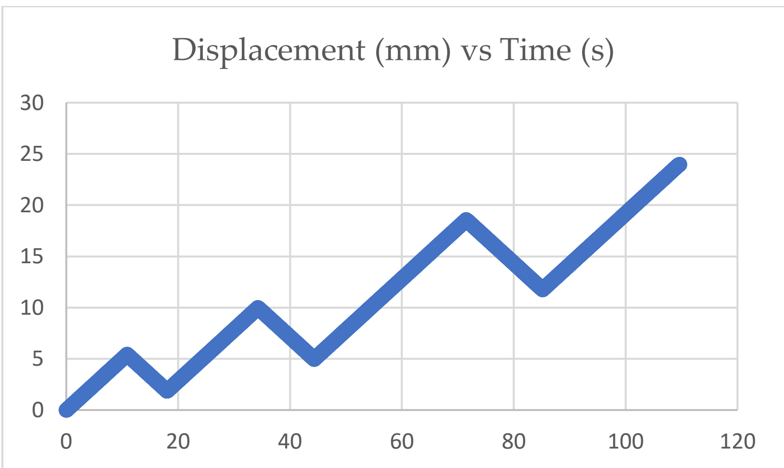

Figure 3. 5 Cyclic Displacement History

The total displacement and extensometer's upper (u_{upper}) and lower grip (u_{lower}) displacement simulation result he simulation result and experimental result n in Figure 3.6.

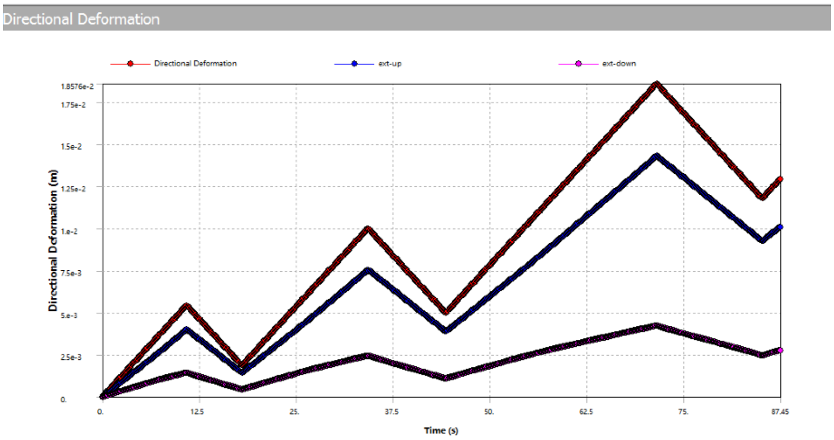

Figure 3. 6 Displacement Simulation

As defined, the gauge length L_0 of extensometer is 50 mm, the engineering strain is calculated as:

$$\varepsilon_{\text{eng}} = \frac{u_{\text{upper}} - u_{\text{lower}}}{L_0} \qquad (3.\ 1)$$

The reaction force $\boldsymbol{F}_{\text{reaction}}$ on the one side face of specimen is plotted in Figure 3.7, the total force applied is twice this value, as the loading force was applied to two faces of the upper grip.

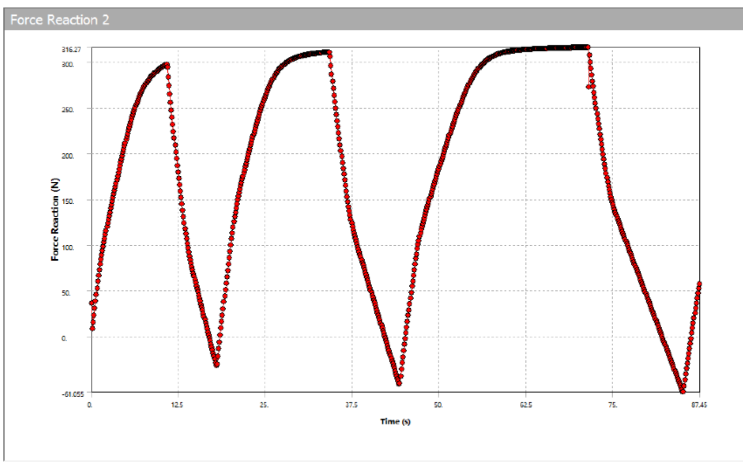

Figure 3. 7 Reaction Force of one face of upper grip

The engineering stress is calculated as:

$$\sigma_{\text{eng}} = \frac{2F_{\text{reaction}}}{A} \qquad (3.\,2)$$

Where A is the cross section area, in this simulation $A = 13 \times 3 = 39\ \text{mm}^2$.

The simulation engineering stress and strain data was imported to MCalibration® and compared to the experimental and MCalibration® calibrated curve. As shown in the figure, the LS-DYNA simulation results closely match the MCalibration® prediction, with the two curves almost overlapping throughout the loading cycles. This indicates that the LS-DYNA implementation of the TNV model successfully reproduces the cyclic tensile response. The hysteresis loops are well captured, demonstrating the model's ability to simulate inelastic and rate-dependent behavior.

A minor deviation is observed during the unloading phase, where the LS-DYNA curve slightly overshoots, with stress dropping into a small compressive range. Nevertheless, the overall trend and deformation behavior are accurately reproduced, confirming the robustness of the calibrated model.

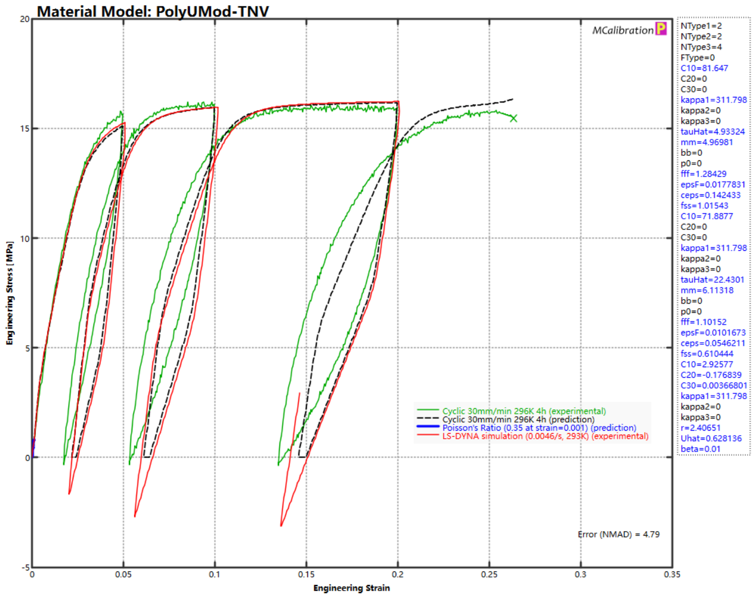

Figure 3. 8 Comparison of Simulation and Experiment Cyclic Loading

3.3. Monotonic High Strain Rate Loading Validation

To validate the material model, a monotonic tensile test at strain rate of 300 mm/min was performed in Workbench and compared to the experimental results. The loading history is shown in Figure 3.9.

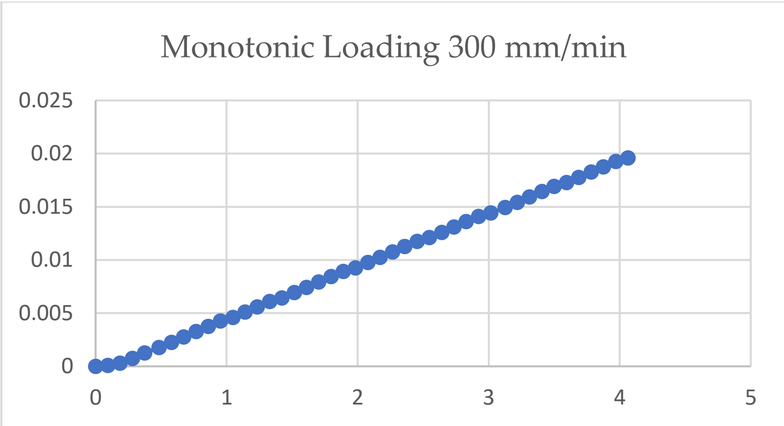

Figure 3. 9 Monotonic 300 mm/min Loading

The simulation and experimental results are shown in Figure 3.10.

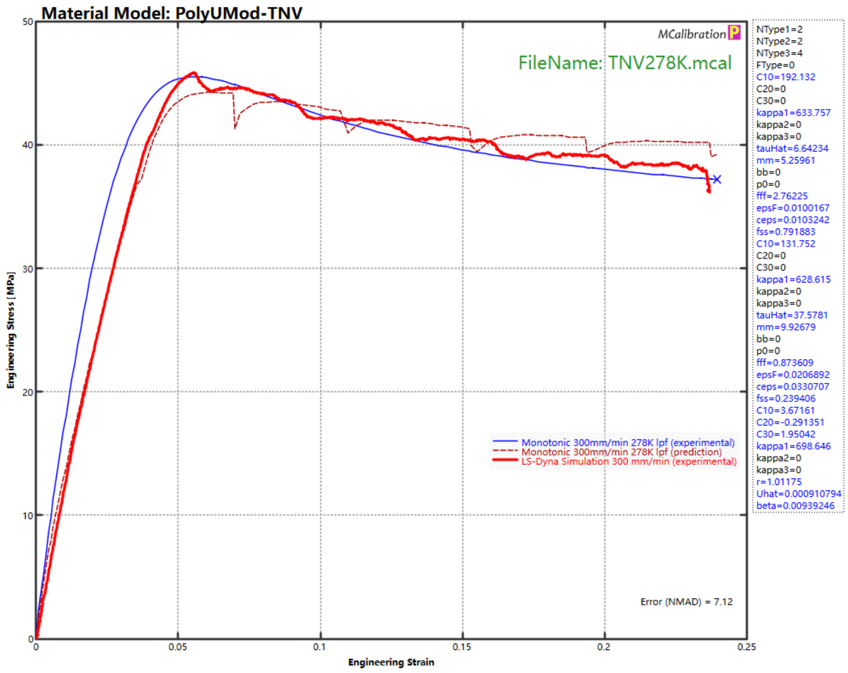

Figure 3. 10 Simulation and Experiment 300 mm/min Comparison

As shown in Figure 3.10, the LS-DYNA simulation result (red solid line) closely follows the experimental data (blue line), particularly in both the elastic and early plastic regimes. The predicted curve from MCalibration® (red dash line), obtained via inverse calibration, also aligns well with the experimental response.

Despite minor fluctuations in the hardening region of the simulation, the overall trend—including the peak stress and post-yield softening—is accurately captured. This demonstrates that the PolyUMod-TNV model, calibrated at this temperature and strain rate, can reliably predict the material's mechanical behavior under monotonic loading.

3.4. Temperature dependence validation

The temperature dependence of the model was implemented through linear interpolation of material parameters, based on their previously identified quasi-linear or piecewise-linear trends with temperature. As such, the accuracy of the interpolated model is strongly influenced by the number and distribution of temperature sampling points used during calibration.

For applications where high precision is not critical, the interpolated model still provides a reasonable approximation of stress–strain behavior. To evaluate this, we constructed a temperature-dependent TNV model in MCalibration® using data at 278 K, 308 K, and 318 K, and applied it to predict the mechanical response at 296 K. The model was validated against experimental data under uniaxial tension and cyclic loading at 30 mm/min. As shown in Figure 3.11, the interpolated model captures the overall trend and magnitude of the stress–strain response, with a normalized mean absolute deviation (NMAD) of 12.6, indicating acceptable accuracy for practical applications. However, the model slightly overestimates the strain hardening behavior, particularly at higher strain levels, which may be attributed to the interpolation between temperature-dependent parameters.

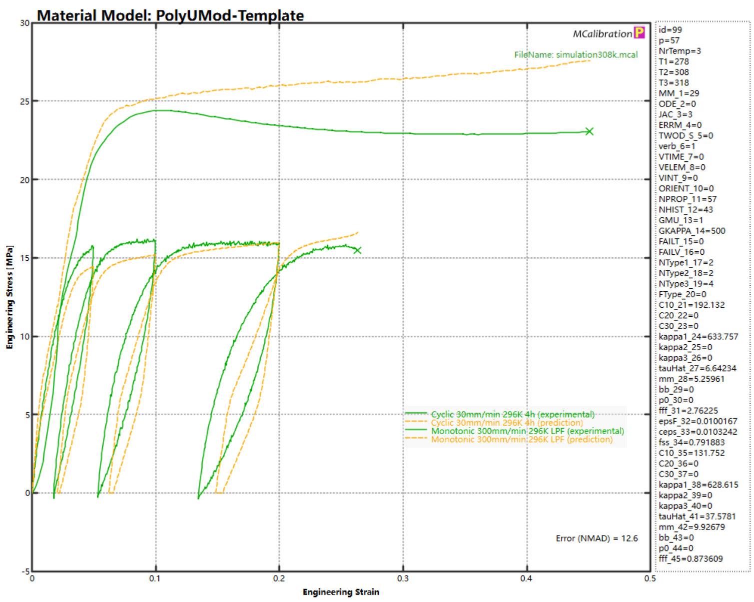

Figure 3. 11 Temperature dependence validation

3.5. Compression Validation

A compression simulation was run in Ansys Ls-dyna, the boundry condition is shown in Figure 3.12.

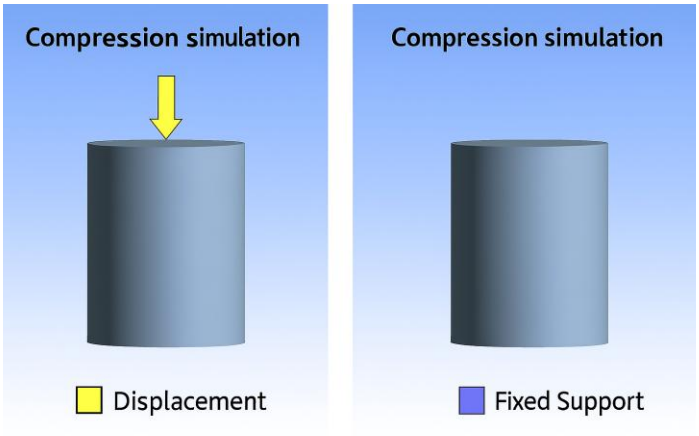

Figure 3. 12 Boundary Condition of Compression

Applying the same displacement history of 296K as compression experiment as boundary condition, then compare the simulation output to experiment result. To simulate compression experiment, it is necessary to insert Hourglass Control, since reduced integration elements can exhibit non-physical zero-energy deformation modes under compression.

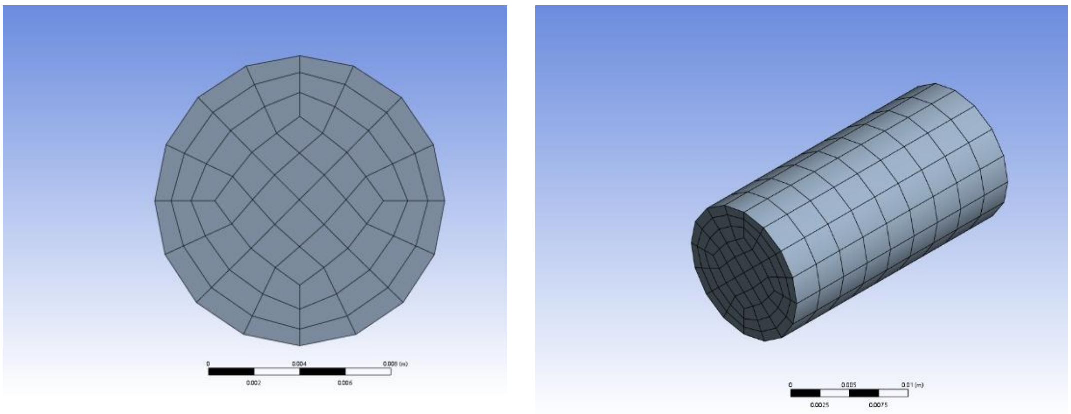

Figure 3. 13 Mesh on ASTM D695 Cylinder Specimen

A structured mesh was generated using the Multi Zone method combined with an inflation layer around the central axis (Figure 3.13). This approach ensures high element quality near the loading surface and maintains axisymmetric regularity throughout the domain. The inflation layers help capture stress gradients near contact interfaces while preserving computational efficiency with hexahedral-dominant elements.

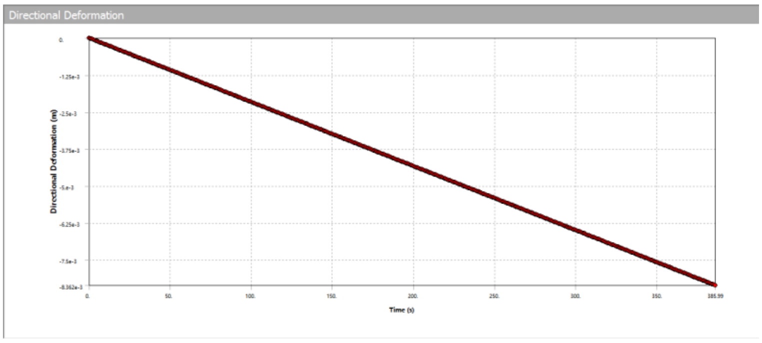

Figure 3. 14 Compression Displacement vs Time

The Energy Summary was shown in Figure 3.15. As shown, the hourglass energy remains below 5% of the total internal energy, indicating that the simulation results are stable and reliable.

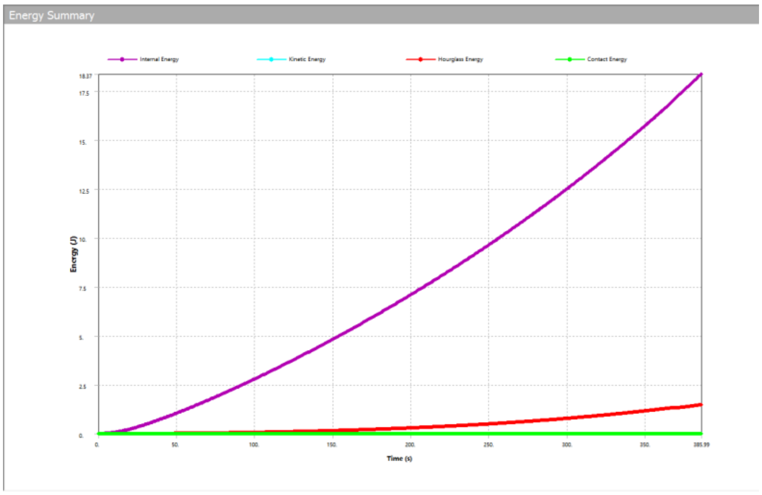

Figure 3. 15 Energy Summary

Figure 3.16 illustrates the deformed shape of the specimen. A slight barreling effect can be observed, but its magnitude is limited, and the influence on the calculated engineering stress is considered negligible.

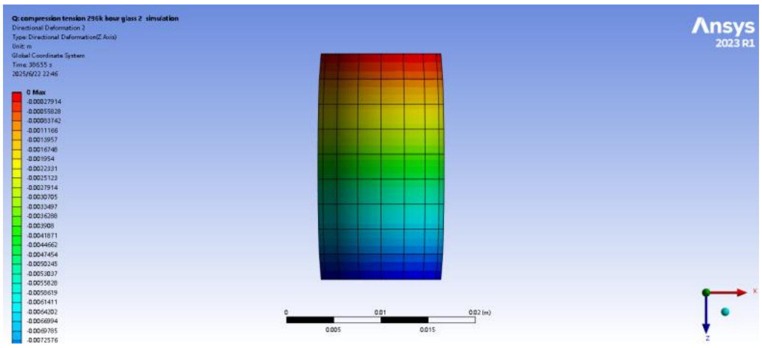

Figure 3. 16 Specimen Deformation

The reaction force obtained from the simulation was exported and compared with the experimental results. As shown in Figure 3.17, the two curves exhibit good agreement, indicating that the numerical model predicts the reaction force with reasonable accuracy. When a refined mesh was applied, the simulation results remained consistent and exhibited improved agreement with the experimental data. Furthermore, the hourglass energy was reduced compared to the case with larger elements, which further supports the validity and numerical stability of the model.

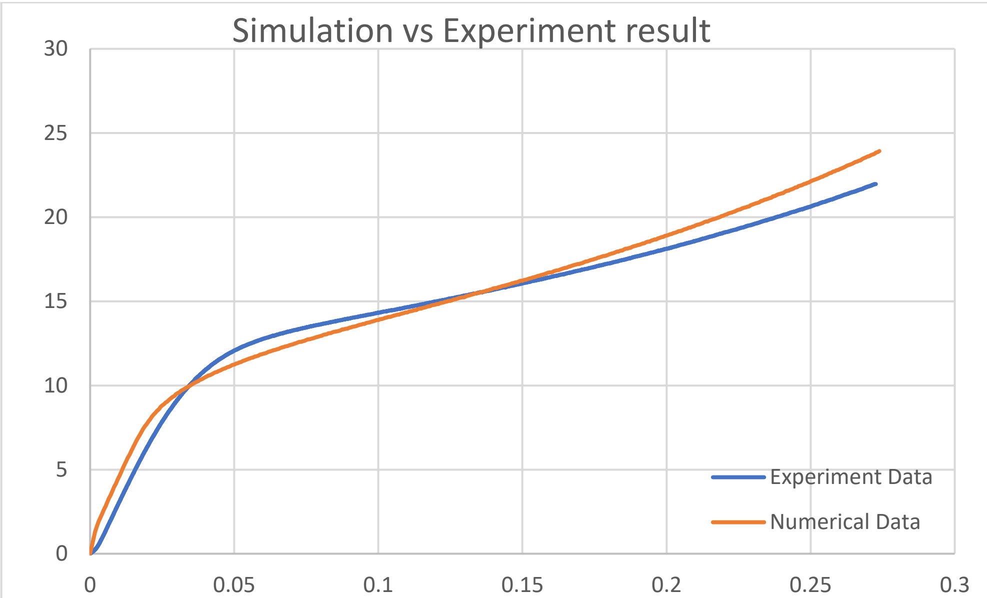

Figure 3. 17 Numerical Result vs Experiment Result

3.6. Three-points Bending Validation

To further validate the accuracy and robustness of the numerical model, a three-point bending simulation was conducted in LS-DYNA. The experimental setup is illustrated in Figure 3.18, where both the punch and support have a radius of 0.5 mm, the span length is 51.2 mm, the specimen thickness is 3.6 mm, and the total specimen length is 137 mm. To eliminate the friction force, the contact surface to the two supports are lubricated by Vaseline.

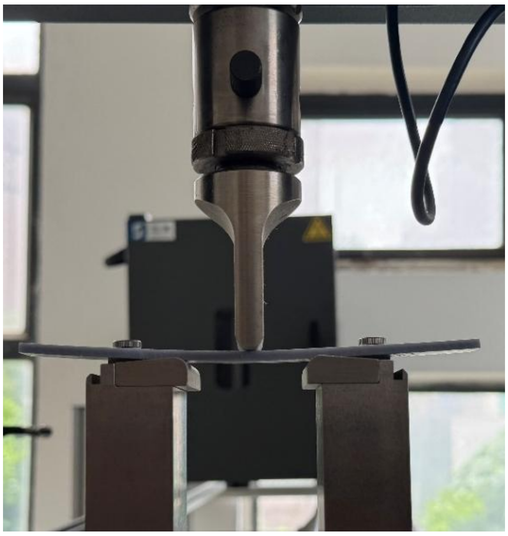

Figure 3. 18 Three-point Bending Set up

In the quasi-static test, the punch was displaced by 5 mm over a duration of 300 seconds, the tests were repeated five times for extracting an average force and displacement relation, the deformed shape of the specimen is shown in Figure 3.19.

Figure 3. 19 Deformed Specimen

Quasi-static analysis replicating the experimental loading conditions was conducted to the numerical model, the complete simulation setup, including boundary conditions and contact definitions, is illustrated in Figure 3.20.

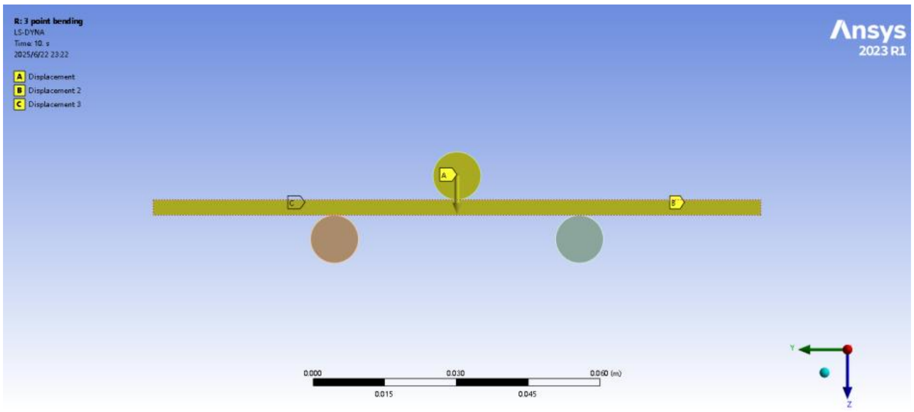

Figure 3. 20 Three Points Bending Simulation

The deformed shape and Equivalent Stress of the specimen after loading is shown in Figure 3.21, where a smooth bending curvature without significant shear distortion can be observed.

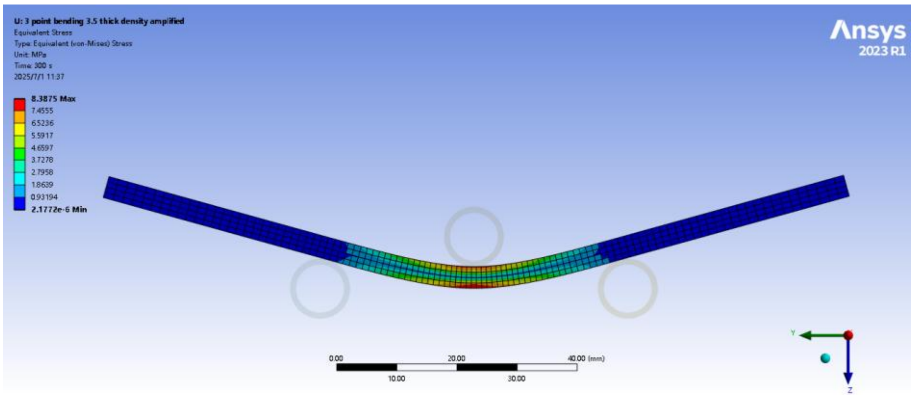

Figure 3. 21 Bending Simulation Equivalent Stress

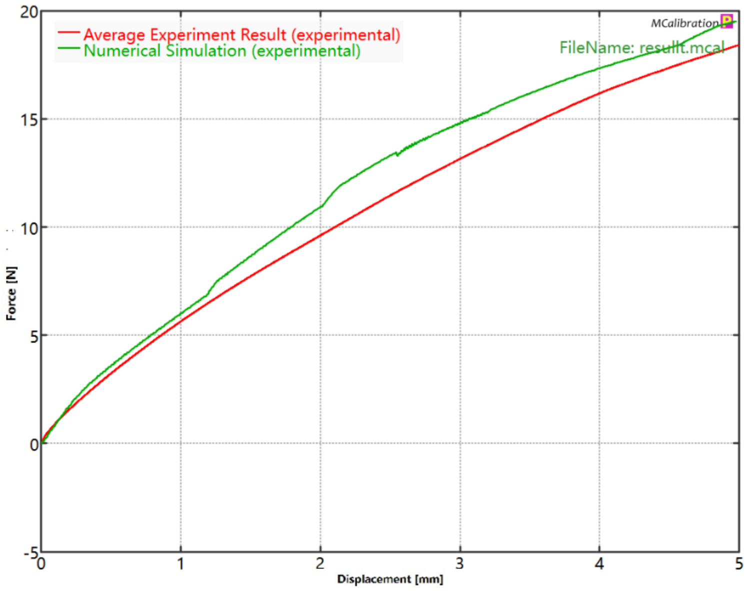

Figure 3. 22 Numerical vs Experiment Contact Force vs Displacement

The numerical and experimental contact force versus axial displacement result is compared in Figure 3.22, showing good overall agreement. It is important to note that, during the experimental procedure, the recorded force and displacement data may contain noise if the support span is too short. In such cases, applying a low-pass filter is recommended to improve data quality. Another critical factor influencing the results is the specimen thickness. Since the contact force is proportional to the second moment of area (also known as the moment of inertia of the cross section), even a 10% increase in thickness can lead to approximately a 33% increase in bending stiffness and, consequently, in the required force. Therefore, maintaining accurate control of specimen thickness is essential in bending experiments.

Overall, the numerical model is capable of accurately reproducing the material behavior observed in experiments under tension, compression, and bending conditions. It can also predict temperature-dependent responses through interpolation. However, if the printing or curing conditions are altered, the material model must be recalibrated accordingly to ensure predictive accuracy.

4 Model Limitation and Further Discussion

The calibrated material model is capable of capturing the general mechanical behaviour of the material. Although its accuracy decreases under high strain rates or at relatively low temperatures, the overall trends are reasonably well predicted. Nevertheless, several limitations and potential improvements are discussed in the following sections.

4.1. Temperature Interpolation Limit

The PolyUMod TNV model applies linear interpolation to material parameters within the experimental temperature range but does not support extrapolation beyond these bounds. This limitation can be avoided by using the ANSYS TN model, which incorporates temperature dependence directly through functional relationships within the material formulation, but it might sacrifice model accuracy.

4.2. Manufacturing Process

The mechanical behavior of photopolymer resins is highly sensitive to a variety of external factors, including color formulation, post-curing duration, and storage conditions. These variables can significantly influence the degree of crosslinking, the balance between stiffness and ductility, and the long-term stability of the material. For instance, gray resin often exhibits effective surface curing but poor interior polymerization due to limited light penetration, while transparent resin cures more uniformly yet is more vulnerable to UV-induced aging. Additionally, curing time plays a critical role: over-curing (e.g., 4 hours) may increase stiffness but leads to embrittlement and a sharp decline in fracture strain, whereas shorter durations (10–20 minutes) preserve better toughness. Improper storage—especially prolonged light exposure—can further accelerate degradation, particularly in transparent samples. Given these sensitivities, the constitutive model developed in this study provides reliable predictive capability for the specific batch and processing conditions under which it was calibrated. However, if significant variations occur in material formulation, printing parameters, or post-processing conditions, recalibration of the model is required to maintain accuracy and reliability [15].

4.3. Slack Adapter and Cushion

In tensile tests at different strain rates, the initial loading stage often deviates from the target strain rate due to the acceleration phase of the load cell. To mitigate this, a slack adaptor is recommended to allow the system to reach the desired velocity before engaging the specimen, thereby ensuring a more accurate initial strain rate. Additionally, to reduce noise and transient effects in the early loading curve, a cushioning layer between the slack adaptor stroke and its shell can be used.

4.4. Material Library and Solver

The PolyUMod TNV model provides the highest fitting accuracy; however, it requires a licensed external material library and must be run with the PolyUMod LS-DYNA solver. In contrast, the built-in ANSYS TN model offers lower accuracy, but does not rely on any external libraries. It serves as a practical alternative when the PolyUMod material library is unavailable or when high precision is not essential.

4.5. Self-heating

One limitation of the current modeling approach is that it does not account for self-heating effects. At higher strain rates or under repeated loading, viscoelastic and viscoplastic dissipation can generate localized temperature rises within the specimen, especially for cylinder specimen. This self-heating can soften the material and alter its mechanical response, particularly by reducing the apparent stiffness and strength in subsequent loading cycles. Since the experimental data were collected without temperature monitoring or thermal control, the model calibration assumes isothermal conditions. As a result, part of the deviation between the model predictions and experimental data, especially under higher strain rates, maybe attributed to the coupled thermo-mechanical effects.

4.6. Virtual Experiment

MCalibration can be integrated with an FEM solver to perform virtual experiments under simple loading histories. In such cases, it internally calls the solver (e.g ANSYS) to compute the material response. As a result, the stress–strain curves obtained from virtual experiments closely match those from standalone FEM simulations. This functionality is particularly useful for quickly predicting material behavior under varying conditions—such as changes in strain rate or temperature—without the need to manually set up full finite element models. However, for more complex scenarios involving real component geometries, boundary conditions, or contact interactions, full finite element simulations in ANSYS are required. While MCalibration provides efficient solver-driven validation for isolated loading paths, it cannot capture full-field mechanical responses under realistic structural conditions.

4.7. Deformation measurement

In this experiment, strain was measured using an extensometer during tensile tests, while crosshead displacement was used to calculate strain in compression tests. This approach considers only axial deformation and neglects lateral strain, which may lead to inaccuracies in estimating the true strain. To improve accuracy, Digital Image Correlation (DIC) can be introduced to capture lateral deformation more precisely, enabling more accurate determination of true stress.

Bibliography

[1] A. Al Rashid, W. Ahmed, M. Y. Khalid, and M. Kog, "Vat photopolymerization of polymers and polymer composites: Processes and applications," Additive Manufacturing, vol. 47, p. 102279, 2021.

[2] R. L. Sælen, O. S. Hopperstad, and A. H. Clausen, "Mechanical behaviour and constitutive modelling of an additively manufactured stereolithography polymer," Mechanics of Materials, vol. 185, p. 104777, 2023.

[3] B. P. Reis, L. M. Nogueira, D. A. Castello, and L. A. Borges, "A visco-hyperelastic model with Mullins effect for polyurethane elastomers combining a phenomenological approach with macromolecular information," Mechanics of Materials, vol. 161, p. 104023, 2021.

[4] H. Kolsky, "Stress waves in solids," Journal of Sound and Vibration, vol. 1, no. 1, pp. 88–110, 1964.

[5] A. Shahin, I. Barsoum, and M. D. Islam, "Constitutive model calibration of the time and temperature-dependent behavior of high density polyethylene," Polymer Testing, vol. 91, p. 106800, 2020.

[6] A. Almomani, S. Deveci, A.-H. I. Mourad, and I. Barsoum, "Constitutive model calibration for the thermal viscoelastic-viscoplastic behavior of high density polyethylene under monotonic and cyclic loading," Polymer Testing, vol. 118, p. 107911, 2023.

[7] H. J. Qi and M. C. Boyce, "Stress–strain behavior of thermoplastic polyurethanes," Mechanics of Materials, vol. 37, no. 8, pp. 817–839, 2005.

[8] Y. Liu, X. Zhang, and J. Wang, "A thermomechanically coupled viscoelastic–viscoplastic model for amorphous polymers," Polymer Testing, vol. 98, p. 106601, 2021.

[9] J. Bergström, Smart Experimental Testing for Material Model Calibration, YouTube video, PolymerFEM, 2022.

[10] Anycubic Resin User Manual & MSDS, Anycubic. [Online]. Available: https://www.anycubic.com/pages/anycubic-resin-user-manual-msds

[11] Z. Liang, J. Li, X. Zhang, and Q. Kan, "A viscoelastic-viscoplastic constitutive model and its finite element implementation of amorphous polymers," Polymer Testing, vol. 117, p. 107831, 2023.

[12] M. Hossain, R. Navaratne, and D. Perić, "3D printed elastomeric polyurethane: Viscoelastic experimental characterizations and constitutive modelling with nonlinear viscosity functions," International Journal of Non-Linear Mechanics, vol. 126, p. 103546, 2020.

[13] J. Yang, Z. Liao, M. Hossain, G. Huang, X. Zhou, F. Liu, A. S. M. Alzaidi, and X. Yao, "Thermo-mechanical properties of digitally-printed elastomeric polyurethane: Experimental characterisation and constitutive modelling using a nonlinear temperature-strain coupled scaling strategy," International Journal of Solids and Structures, vol. 267, p. 112163, 2023.

[14] G. Luo, C. Wu, K. Xu, L. Liu, and W. Chen, "Development of dynamic constitutive model of epoxy resin considering temperature and strain rate effects using experimental methods," Mechanics of Materials, vol. 159, p. 103887, 2021.

[15] M. Heidari Pebdani, R. Janisch, and F. Pyczak, "Generalized pole figures from post-processing whole Debye–Scherrer patterns for microstructural analysis on Ti–Al-based alloys with Mo," Materials Characterization, vol. 185, p. 111712, 2022.

[16] S. H. Mian, U. Umer, K. Moiduddin, and H. Alkhalefah, "Predicting Mechanical Properties of Polymer Materials Using Rate-Dependent Material Models: Finite Element Analysis of Bespoke Upper Limb Orthoses," Polymers, vol. 15, no. 21, p. 4572, 2023.

A Appendix A

A.1. Material Card of PolyUMod TNV model

Material Card 1 PolyUMod TNV model Multi Temperature Frame

```
*MAT_USER_DEFINED_MATERIAL_MODELS
$# -- MCalibration defined material model -- start
$# Units: [length]=millimeter, [force]=Newton, [time]=seconds, [temperature]=Kelvin
$# Material Model: PolyUMod-Template
$# Calibration file name: Untitled
$#    mid       ro       mt      lmc      nhv   iortho    ibulk       ig
        1 1.15e-06       45       48       52        0       14       13
$#  ivect    ifail       it   ihyper     ieos     lmca
        0        1        1        1        0      187
$#     id        p   NrTemp       T1       T2       T3       T4     MM_1
       99       57        4      278      296      308      318       29
$#  ODE_2    JAC_3   ERRM_4 TWOD_S_5   verb_6  VTIME_7  VELEM_8   VINT_9
        0        3        0        0        1        0        0        0
$#  ORIENT_1  NPROP_11  NHIST_12    GMU_13 GKAPPA_14  FAILT_15  FAILV_16 NType1_17
        0       57       43        1      500        0        0        2
$# NType2_1 NType3_19 FType_20   C10_21   C20_22   C30_23 kappa1_24 kappa2_25
        2        4        0  192.132        0        0  633.757        0
$# kappa3_2 tauHat_27    mm_28    bb_29    p0_30   fff_31   epsF_32   ceps_33
        0  6.64234  5.25961        0        0  2.76225 0.0100167 0.0103242
$# fss_34   C10_35   C20_36   C30_37 kappa1_38 kappa2_39 kappa3_40 tauHat_41
  0.791883  131.752        0        0  628.615        0        0  37.5781
$#  mm_42    bb_43    p0_44   fff_45   epsF_46   ceps_47   fss_48   C10_49
   9.92679        0        0 0.873609 0.0206892 0.0330707 0.239406  3.67161
$# C20_50   C30_51 kappa1_52 kappa2_53 kappa3_54     r_55   Uhat_56  beta_57
 -0.291351  1.95042  698.646        0        0  1.01175 0.0009108 0.0093925
$#  MM_58   ODE_59   JAC_60  ERRM_61 TWOD_S_62   verb_63 VTIME_64 VELEM_65
       29        0        3        0        0        1        0        0
$# VINT_66 ORIENT_67 NPROP_68 NHIST_69   GMU_70 GKAPPA_71 FAILT_72 FAILV_73
        0        0       57       43        1      500        0        0
$#NType1_7 NType2_75 NType3_76 FType_77   C10_78   C20_79   C30_80 kappa1_81
        2        2        4        0   81.647        0        0  311.798
$#kappa2_8 kappa3_83 tauHat_84    mm_85    bb_86    p0_87   fff_88  epsF_89
        0        0  4.93324  4.96981        0        0  1.28429 0.0177831
$# ceps_90   fss_91   C10_92   C20_93   C30_94 kappa1_95 kappa2_96 kappa3_97
  0.142433  1.01543  71.8877        0        0  311.798        0        0
$#tauHat_9    mm_99   bb_100   p0_101  fff_102 epsF_103 ceps_104 fss_105
   22.4301  6.11318        0        0  1.10152 0.0101673 0.0546211 0.610444
```

```
$# C10_106   C20_107   C30_108 kappa1_10 kappa2_11 kappa3_11     r_112  Uhat_113
   2.92577 -0.176839  0.003668   311.798        0        0  2.40651  0.628136
$#beta_114    MM_115   ODE_116   JAC_117  ERRM_118 TWOD_S_11  verb_120 VTIME_121
      0.01        29         0         3         0         0         1         0
$#VELEM_12    VINT_123  ORIENT_12  NPROP_125  NHIST_126      GMU_127  GKAPPA_12
FAILT_129
         0         0         0        57        43         1       500         0
$#FAILV_13 NType1_13 NType2_13 NType3_13 FType_134   C10_135   C20_136   C30_137
         0         2         2         4         0  47.3552         0         0
$#kappa1_1 kappa2_13 kappa3_14 tauHat_14    mm_142    bb_143    p0_144   fff_145
   122.979         0         0  4.84817   3.92144         0         0  2.63355
$#epsF_146  ceps_147   fss_148   C10_149   C20_150   C30_151 kappa1_15 kappa2_15
   0.93856  0.134783  0.843048   16.2821         0         0   122.979         0
$#kappa3_1 tauHat_15    mm_156    bb_157    p0_158   fff_159  epsF_160  ceps_161
         0   9.00127   5.14651         0         0   1.99575   2.49965   0.13713
$# fss_162   C10_163   C20_164   C30_165 kappa1_16 kappa2_16 kappa3_16     r_169
  0.812234   2.22539  0.250053  0.167238   122.979         0         0  2.06392
$#Uhat_170  beta_171    MM_172   ODE_173   JAC_174  ERRM_175 TWOD_S_17  verb_177
  0.084644 0.0148951        29         0         3         0         0         1
$#VTIME_17  VELEM_179    VINT_180  ORIENT_18  NPROP_182  NHIST_183      GMU_184
GKAPPA_18
         0         0         0         0        57        43         1       500
$#FAILT_18 FAILV_187 NType1_18 NType2_18 NType3_19 FType_191   C10_192   C20_193
         0         0         2         2         4         0   31.7081         0
$# C30_194 kappa1_19 kappa2_19 kappa3_19 tauHat_19    mm_199    bb_200    p0_201
         0   74.1175         0         0   2.46029   2.78534         0         0
$# fff_202  epsF_203  ceps_204   fss_205   C10_206   C20_207   C30_208 kappa1_20
   2.59763 0.0101758  0.341005  0.226895   5.40567         0         0   74.1175
$#kappa2_2 kappa3_21 tauHat_21    mm_213    bb_214    p0_215   fff_216  epsF_217
         0         0   3.02863   4.75891         0         0   2.00885  0.513859
$#ceps_218   fss_219   C10_220   C20_221   C30_222 kappa1_22 kappa2_22 kappa3_22
 0.0105977  0.602757   1.98664  -1.19339   1.99393   74.1175         0         0
$#   r_226  Uhat_227  beta_228
   1.16316   2.79684 0.0215754
$# -- MCalibration defined material model -- end
```

List of Figures

List of Tables

List of symbols

Variable	Description	SI Unit
$\boldsymbol{F}$	Total deformation gradient tensor	
$\boldsymbol{F_e}^{(n)}$	Elastic deformation gradient of network *n*	
$\boldsymbol{b_e}^{(n)*}$	Isochoric part of left Cauchy-Green tensor	
$J_e^{(n)}$	Elastic volume ratio of network *n*	
$\lambda_e^{(n)*}$	Effective chain stretch in network *n*	
σ	Cauchy stress tensor	MPa
κ	Bulk modulus	MPa
μ	Shear modulus	MPa
C_{10}, C_{20}, C_{30}	Yeoh hyperelastic material constants	MPa
$\hat{\tau}$	Reference flow stress parameter	MPa
$\dot{\gamma}$	Equivalent shear strain rate	s^{-1}
m	Strain rate sensitivity exponent	
n	Temperature sensitivity exponent	
$R(p)$	Ramp function: *(p +	p
$P0$	Hydrostatic pressure	MPa
θ	Temperature	K
θ_0	Reference temperature	K

Variable	**Description**	**SI Unit**
$L^{-1}(x)$	Inverse Langevin function	
ε_e	Engineering strain	
σ_{eng}	Engineering stress	MPa
A	Cross-sectional area	mm^2
γ_0	Reference shear rate	s^{-1}
NMAD	Normalized Mean Absolute Deviation	

Acknowledgments

First and foremost, I would like to express my deepest gratitude to my supervisor, Prof. Antonio Mattia Grande, for his invaluable guidance, encouragement, and insightful feedback throughout the course of this thesis. His expertise and clear direction have been instrumental in shaping both the technical depth and academic rigor of this work.

I would also like to sincerely thank Dr. Bianca Omede, whose continuous support and constructive advice have helped me overcome numerous challenges during my research. Her attention to detail and thoughtful discussions have been truly appreciated.

Furthermore, I wish to acknowledge the resources and facilities provided by Politecnico di Milano, which made the experimental and computational work possible.

Last but not least, I am grateful to my family and friends for their unwavering support, patience, and motivation during this demanding yet rewarding journey.